Motion Response Characteristics of a Kyushu-University Semi- Submersible Floating Wind Turbine with Trussed Slender Structures: Experiment vs. Numerical Simulation

Liu, Yingyi
Research Institute for Applied Mechanics, Kyushu University

Hu, Changhong
Research Institute for Applied Mechanics, Kyushu University

Sueyoshi, Makoto
Research Institute for Applied Mechanics, Kyushu University

Yoshida, Shigeo
Research Institute for Applied Mechanics, Kyushu University

他

出版情報：Ocean Engineering. 232 (109078), 2021-07-15. Elsevier
バージョン：
権利関係：

Motion Response Characteristics of a Kyushu-University Semi-Submersible Floating Wind Turbine with Trussed Slender Structures: Experiment vs. Numerical Simulation

Yingyi Liu [a,], Changhong Hu [a], Makoto Sueyoshi [a], Shigeo Yoshida [a], Hidetsugu Iwashita [b], Masashi Kashiwagi [c]*

[a] *Research Institute for Applied Mechanics, Kyushu University, Fukuoka, 8168580, Japan*
[b] *Department of Transportation and Environmental Systems, Hiroshima University, Hiroshima, 7398527, Japan*
[c] *Department of Naval Architecture & Ocean Engineering, Osaka University, Osaka, 5650871, Japan*

Emails: *liuyingyi@riam.kyushu-u.ac.jp (Y. Liu); hu@riam.kyushu-u.ac.jp (C. Hu); sueyoshi@riam.kyushu-u.ac.jp (M. Sueyoshi); yoshidas@riam.kyushu-u.ac.jp (S. Yoshida); iwashita@naoe.hiroshima-u.ac.jp (H. Iwashita); kashi@naoe.eng.osaka-u.ac.jp (M. Kashiwagi)*

* Correspondence e-mail: liuyingyi@riam.kyushu-u.ac.jp; Tel.: +81-80-8565-7934

Received: date; Accepted: date; Published: date

Abstract: Understanding the dynamics of an FWT (Floating Wind Turbine) is essential for its design and operation. Since a truss structure can reduce the wave load/resistance on the floating foundation, it becomes more and more popular in industrial applications. In this regard, knowing the effect of slender members of the truss structure on the motion response characteristics of such an FWT is vital. The present work develops a time-domain method for modeling the dynamics of a floating truss-structure wind turbine with multiple rotors on the deck of the platform. In its hydrodynamic aspect, a hybrid panel-stick model is built up incorporating the potential flow theory to calculate the wave inertia force and a Morison strip method to calculate the wave drag force. A systematic methodology, and the corresponding efficient tool, have been developed to deal with the floating truss-structure consisting of a set of slender cylindrical members in arbitrary lengths, diameters, orientations, and locations. The Morison dynamic solver is incorporated into the time-domain solver for the FWT dynamics. The proposed model is validated against a model experiment of a semi-submersible FWT with a triangular-shaped truss-structured platform, which was carried out in RIAM (Research Institute for Applied Mechanics), Kyushu University. Good agreements between the simulation results and the experimental data confirm the validity of the developed method. Further numerical simulations are performed in a set of wind and wave conditions to investigate the effect of wave drag force on the FWT dynamics. It is found that without the fluid viscosity, resonant responses are excited in the platform motions at frequencies that are close to the natural frequencies of the FWT system. Via a comparison between the parked conditions and operating conditions of the FWT, it is found that in the presence of steady wind, the translational surge or sway motion is significantly excited at its resonance frequency. This may be attributed to the work done by the wind to the FWT, which enhances remarkably the total kinetic energy of the platform and consequently increases the translational surge or sway velocity of the platform at the equilibrium position. Applying a hybrid panel-stick model will be effective in reducing all these non-realistic large resonant responses.

Keywords: trussed structure; slender bracings; catenary mooring system; viscous damping; motion response analysis; hybrid model.

1. Introduction

Offshore wind turbine offers a promising solution to harnessing the abundant wind resources. With the development of technology, the offshore wind turbine industry is gradually moving from shallow water to intermediate water and deepwater. As one of the three mainstream concepts of the floating foundation to keep stability, the semi-submersible type has a smaller surge response than the TLP (Tension Leg Platform) type and a smaller pitch response than the spar type (Li et al., 2011; Goupee et al., 2014). The installation cost of the mooring system of a semi-submersible foundation is also relatively lower than the other types of floating foundations (Liu et al., 2016c).

As a consequence, in the past decade, several important configurations of the semi-submersible type have been proposed, e.g., the WindFloat™ (Roddier et al., 2010), DeepCwind (Robertson et al., 2014), WINFLO™ (Boulluec et al., 2013), etc. Researches have been undertaken on various aspects of the semi-submersible concept, involving model testing (Robertson et al., 2017; Kim et al., 2017; Li et al., 2018; Koch et al., 2018), numerical modeling and conceptual study (Bae et al., 2014; Bayati et al., 2014; Karimirad and Michailides, 2015 and 2016; Liu et al., 2018) as well as other aspects relevant to the uncertainty analysis, the control design, and the fatigue prevention, etc. (Zhu et al., 2016; Wang et al., 2016; Uzunoglu et al., 2018; Liu et al., 2018). Typically, these semi-submersible foundations have three or four columns to provide the main buoyancy force and some other small, slender members to support the stiffness of the entire structure.

An important issue of the semi-submersible foundations is the prediction of their motion responses, among which the heave response may be of particular concern. At a special frequency, i.e., the near-zero-excitation frequency, the wave excitation force can almost disappear at the equilibrium position during the heave motion. Faltinsen (1990) stated that in beam seas, the heave natural frequency should be larger than its near-zero-excitation frequency. This conclusion was later confirmed by Newman (1999). Newman (1999) also proved that in the long-wavelength regime, the heave RAO (Response Amplitude Operator) approaches unity. At the natural frequencies, when using a potential flow-based method, the semi-submersible normally endures remarkable resonant responses. The reason lies in that, in fact, near the boundary layer of the submerged part of the floating structure, the wave-induced drag force (which is a viscous force) has not been accounted for as that is usually done in an N-S (Navier-Stokes) equation-based solver. Expected discrepancies can be found in the computation results of the 6-DoF (Degree of Freedom) motion responses of an FWT between a potential flow-based method and a CFD (Computational Fluid Dynamics) method (Nematbakhsh et al., 2015).

To include the viscous effect, the potential flow-based method needs to be modified to some extent. Sarpkaya (2015) investigated the relative dominant wave loading regimes for a circular cylinder, which was also listed in Benitz et al. (2015), and discovered that the wave diffraction theory is only strictly valid for the region of $\pi D/L < 0.5$ (in which D is the diameter of the cylinder and L is the wavelength); outside of this region, the wave drag force needs to be considered. Other than solving the N-S equation, which is extremely time-consuming and cost-expensive, an alternative way is to employ a hybrid approach combing the potential flow theory and the Morison equation (Li and Yu, 2012). A list of numerical methods is given in Table 1, which are primarily based on the potential flow theory and the Morison equation, with the aid of various modeling tools. These methods apply various hybrid methodologies for modeling the hydrodynamics of the floating platform, taking into consideration where to account for the diffraction-radiation effect and where to account for the viscous effect. By performing numerical simulations for different concepts of semi-submersible FWTs, almost all of these researches confirmed that inclusion of the Morison counterpart as a supplement to the potential flow-based methods could result in more reasonable predictions for the dynamic responses of semi-submersible FWTs, especially those having plenty of slender bracings.

Table 1. A review of numerical methods for modeling a semi-submersible FWT

Authors	Potential Flow Method	Morison Method	Hybrid Methodology	FWT Modeling Software	FWT Model
Kvittem et al. (2012)	BEM (WADAM™)	Time domain	BEM for all members (inertia), Morison for some members (drag)	SIMO™/RIFLEX™	FWT similar to WindFloat™
Ledru et al. (2014)	BEM (Diodore™)	Time domain	BEM for columns (inertia), Morison for the other members (inertia + drag)	DeepLines™	OC4 DeepCwind FWT©
Tran & Kim (2015)	BEM (AQWA™)	Time domain	BEM for columns and plates (inertia), Morison for bracings (drag)	AQWA-Line™ /AQWA-NAUT™	OC4 DeepCwind FWT©
Wendt et al. (2015)	BEM (WAMIT™)	Time domain	BEM for all members (inertia), Morison for all members (drag)	HydroDyn© /FAST©	OC4 DeepCwind FWT©
Liu et al. (2015)	BEM (HAMS©)	Frequency domain	Two hybrid modeling strategies were introduced and compared	-	Kyushu-University FWT©
Ishihara & Zhang (2019)	-	Time domain	Morison for all members (inertia + drag)	inhouse code	Not mentioned
Present method	BEM (HAMS©)	Time domain	BEM for all members (inertia), Morison for all members (drag)	inhouse code	Kyushu-University FWT©

The Morison equation can be easily applied to a monopile or Spar because of its simple regular geometry. However, in respect to a complex truss structure with a great number of braces, as shown in Figure 1, unlike the braceless type (e.g., Karimirad and Michailides, 2015; 2016), one needs to develop a systematic methodology to take into consideration of all geometric specifications, i.e., the diameters, lengths, orientations, and locations of all members. It may involve the development of a Morison mesh generator and a Morison dynamic solver. Based on the study in Liu et al. (2015), an appropriate way of hybrid modeling is to apply BEM (Boundary Element Method) for the inertia part of wave force while using the Morison method for the drag part on all the members. Such a way can substantially improve the computation efficiency but avoid double-counting the fluid inertia and the wave excitation (Tran & Kim, 2015). Besides, although many of the previous researches studied the effect of viscous wave loading on the floating platform of an FWT in parked status, rare research concerns the impact of viscous wave loading on the platform under the circumstance of FWT operation. Indeed, it is crucial to investigate the role that the wave drag force takes in affecting the motion of an FWT in the presence of wind. In particular, whether wind matters or not in this process and what is the specific role of wind need to be understood as clearly as possible. For this purpose, the present work tries to fulfill this gap and answer the above questions.

The present work focuses on the prediction and analysis of the motion responses of such a complex semi-submersible with truss members and the understanding of its associated phenomena. A time-domain method is going to be developed to simulate a multi-rotor FWT system, which involves a newly developed hybrid panel-stick method using the strategy mentioned above. Wake effect from the upstream wind turbine will also be considered by using Jensen's model (Jensen, 1983; Katic et al., 1986). Following a validation with the experimental model test, a systematic investigation using the numerical method will be undertaken to study the role of the wave drag force on the semi-submersible FWT with and without the existence of wind. Conclusions will consequently be drawn based on the preceding analysis.

2. The Prototype FWT in Kyushu University

In recent years, a multi-rotor FWT has been proposed in Kyushu University, which is one of the projects in the spotlight in Japan. In the design, a number of slender cylindrical braces are included

to reduce the high wave loading as well as to bring down the cost. To maximize the absorption of the wind power, three wind turbines are installed atop the primary columns of the floating foundation (Hu et al., 2014; Liu et al., 2016). As a multi-purpose floating marine renewable energy system, solar panels are simultaneously installed at its large-space deck, as shown in Figure 1, from which the generated electricity can be used by the surrounding aquaculture farm as well. The layout of the mooring system and the definition of the coordinate system are displayed in Figure 2. Specifications of the prototype are listed in Table 2.

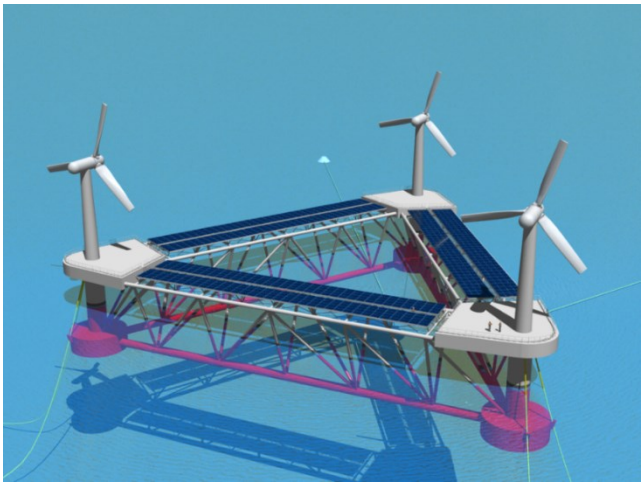

Figure 1. 3D computer graph of a triangular offshore renewable energy system developed in Kyushu University. Slender truss braces are used to strengthen the floating structure and reduce the wave loading acting upon the platform.

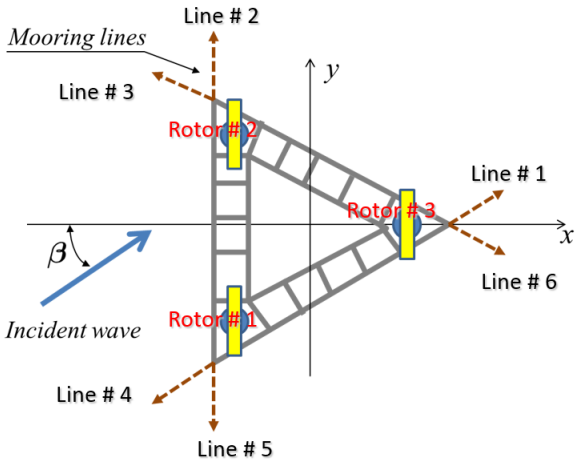

Figure 2. The layout of the mooring system of the semi-submersible FWT. The origin of the coordinate system for the subsequent analysis locates at the planar center of the triangular platform at MSL (Mean Sea Level).

Table 2. Definition of full-scale properties of the semi-submersible

Rotor Diameter	23.38 m
Rated Power for Each Turbine	350 kW
Hub Height above MSL	33.00 m
Platform Mass	2.17×10^{6} kg
Mass of Tower and Nacelle for Each Turbine	9.25×10^{4} kg

Total Draft	10.00 m
Platform Displacement	2.12×10^3 m^3
Number of Mooring Lines	6
Angle between Adjacent Lines	60.00 degree
Water Depth (Depth of Anchor)	70.00 m
Depth of Fairlead below MSL	7.00 m
Radius to Anchor from Fairlead	200.00 m
Radius to Fairlead from CM	51.96 m
Unstretched Mooring Line Length	200.00 m
Mooring Line Diameter	0.06 m
Equivalent Mooring Line Mass Density	68.6 kg/m
Equivalent Mooring Line Stiffness	1.38×10^6 N

3. Time Domain Simulation Method for a Floating Offshore Wind Turbine System

3.1. Motion Equation of the Semisubmersible in Time Domain

In the aforementioned FWT system, wave force and wind force are generally the two main external dynamic forces which the system experiences throughout the entire operation lifetime. Besides, as a major source of the restoring force, the mooring tension loads can keep the floating system from being drifted away under the action of waves and winds. Since the members of the structure are of small aspect ratios, viscous loading in the form of drag force also serves an important role in restraining the motion response, especially in the neighborhood of the resonant periods of the system. Therefore, the motion time history for the integrated floating system can be described by the following equation based on the work of Jonkman (2007):

$$\left[M_{ij} + A_{ij}(\infty)\right]\ddot{\xi}_j(t) + \int_0^t K_{ij}(t-\tau)\dot{\xi}_j(\tau)d\tau + C_{ij}\xi_j(t)$$

$$= F_i^{Wind}(t) + F_i^{Wave}(t) + F_i^{Mooring}(t) + F_i^{Viscous}(t),\ (i,j = 1\sim6), \quad (1)$$

where M_{ij}, C_{ij} are the mass matrix and the restoring matrix of the floating body, respectively; K_{ij} is the retardation function that can be calculated through the cosine transformation of the damping coefficient $B_{ij}(\omega)$

$$K_{ij}(t) = \frac{2}{\pi}\int_0^\infty B_{ij}(\omega)\cos\omega t\, d\omega, \quad (2)$$

$A_{ij}(\infty)$ is the infinite-frequency limit of the added mass $A_{ij}(\omega)$

$$A_{ij}(\infty) = A_{ij}(\omega) + \frac{1}{\omega}\int_0^\infty K_{ij}(t)\cos\omega t\, dt, \quad (3)$$

The Filon quadrature method (Xiang, 2007)) is chosen to compute the Fourier integrals with good accuracy. The forces at the right-hand side of Eq. (1) correspond to the wind loads, the wave excitation loads, the mooring tension loads, and the viscous loads, respectively. The hydrodynamic quantities can be solved by a standard frequency-domain solver (Liu et al., 2018a; 2019), based on the assumption that the fluid is incompressible, irrotational, and inviscid. The hydrodynamic wave excitation loads acting on the floating platform in the time domain can, therefore, be represented by a convolution of the wave

elevation and the non-causal impulse response function, where the latter is determined by the Fourier transform of the wave excitation forces in the frequency domain (Liu et al., 2014).

The mooring tension loads are found at each time step by the solution of an extended catenary theory (Jonkman, 2009) via the Newton-Raphson iteration method, which is capable of considering the seabed friction to the mooring lines. Due to the small diameters of the cylindrical structures of the complex platform in comparison to the wavelength, it is essential to include a supplemental model to account for the viscous correction for the potential flow theory. A Morison-stick model was therefore formulated in the frequency domain (Liu et al., 2016), and is reformulated here in the time domain (Section 4.1 and 4.2).

3.2. Aerodynamics of the Multiple Rotors

The BEMT (Blade Element Momentum Theory), which assumes that the blades can be divided into small annular elements that operate aerodynamically as two-dimensional airfoils (Moriarty and Hansen, 2005), is applied to the aerodynamics computation of each rotor. The crucial step of the BEMT is to find the axial induction factor and the tangential induction factor via a standard iterative procedure. Let the thrust load derived respectively from the momentum theory and the blade element theory be equalized, the axis induction factor a and the tangential induction factor a' can be therefore deduced as follows

$$a = 1/\left(1 + \frac{4F\sin^2\varphi}{\sigma C_n}\right), \tag{4}$$

$$a' = 1/\left[-1 + \frac{4F\sin\varphi\cos\varphi}{\sigma C_t}\right], \tag{5}$$

where F is the product of the tip-loss factor and the hub-loss factor, C_n and C_t are the lift and the drag coefficients of a local blade element, φ is the local flow angle, and σ is the local solidity. To compensate for the deficiency when the rotor enters into the turbulent wake state, the Glauert correction (Spera, 1994) is employed. After resolving the distribution of the normal and the tangential loads along the span of blades, the total thrust force and the shaft torque are obtained by integrations assuming a linear variation (Hansen, 2008) of the load distribution between neighboring blade elements.

Note that there exist multiple rotors on the deck of the semi-submersible floating foundation, and the interactions between the rotors can significantly affect the loadings from the wind. To reflect this phenomenon efficiently, the Jensen's wake model (Jensen, 1983; Katic et al., 1986), also known as the 'Park model', is utilized in the present study. Its empirical equation is based on the conservation of momentum to model a single wake. It is valid for the downstream distance approximately above one rotor diameter in the far wake region. The wind speed in the wake can be expressed as

$$U_w(x) = U_\infty\left(1 - \frac{1-\sqrt{1-C_{T,b}}}{(1+2k_w x/D_{rotor})^2}\right), \tag{6}$$

where D_{rotor} is the rotor diameter, k_w is the wake decay constant, and x is the distance behind the upstream rotor. Typical values for k_w range from 0.04 for offshore (Barthelmie et al., 2010) to 0.075 for onshore cases (Barthelmie et al., 2005). The wake decay constant sets the linear rate of wake expansion with the distance in the streamwise direction. The diameter of the wake expansion is therefore given by

$$D_w = D_{rotor} + 2k_w x. \tag{7}$$

3.3. Modeling of the Catenary Mooring System

In mild sea conditions, the mooring line dynamics can often be described by a linearized relationship to the displacement of the floating support platform. In general, however, the mooring system dynamics are not linear. Instead, nonlinearities are generally evident in the force-displacement

relationships. For the semi-submersible FWT, as shown in Figure 1, the application of an appropriate catenary theory is necessary. Because the traditional catenary theory could not explain the effect of the seabed interaction with a mooring cable in the case it touches the seabed, an improved method proposed by Jonkman (2009) is used in this work, which is capable of accounting for the above issue.

The analytical model, which is given in terms of two unknown variables, i.e., the horizontal and the vertical components of the effective tension in each mooring line at the fairlead, is formulated as follows

$$x_F(F_H,F_V) = L - \frac{F_V}{w} + \frac{F_H}{w} ln\left[\frac{F_V}{F_H} + \sqrt{1+\left(\frac{F_V}{F_H}\right)^2}\right] + \frac{F_H L}{EA} + \frac{C_B w}{2EA}\left[-\left(L-\frac{F_V}{w}\right)^2 + \left(L-\frac{F_V}{w}-\frac{F_H}{C_B w}\right) MAX\left(L-\frac{F_V}{w}-\frac{F_H}{C_B w}, 0\right)\right], \tag{8}$$

$$z_F(F_H,F_V) = \frac{F_H}{w}\left[\sqrt{1+\left(\frac{F_V}{F_H}\right)^2} - \sqrt{1+\left(\frac{F_V - wL}{F_H}\right)^2}\right] + \frac{1}{EA}\left(F_V L - \frac{wL^2}{2}\right), \tag{9}$$

where x_F and z_F are respectively the horizontal and vertical coordinates of the fairlead position relative to the anchor, F_H and F_V are the horizontal and vertical components of the effective tension in the mooring line at the fairlead, w is the mass of the mooring line per unit length, L is the total unstretched mooring line length, C_B is the drag coefficient of seabed static-friction, and EA is the sectional stiffness of the mooring line. It is worth noting that Equations (8) and (9) should be solved iteratively in the local coordinate system via the Newton–Raphson method, etc.

3.4. Solution of the Time-Domain Motion Equation

Several numerical integration methods can solve a differential equation of the second order in the time domain, such as the Newmark-Beta scheme (Wikipedia, 2020a), Adams-Moulton scheme (Wikiversity, 2020b), Adams-Bashforth scheme (Wikiversity, 2020b) and Runge-Kutta scheme (Wikipedia, 2020c). Herein the fourth-order Runge-Kutta scheme is selected to find the solution of Eq. (1) as it can acquire as more as enough accuracy (Ran, 2000; Li and Teng, 2002). Let us consider the time-domain motion equation in the form of $\{\ddot{\xi}\} = Q\left[t, \{\xi\}, \{\dot{\xi}\}\right]$, i.e.,

$$Q\left[t, \{\xi(t)\}, \{\dot{\xi}(t)\}\right] = [\boldsymbol{M}+\boldsymbol{A}]^{-1}\left\{-\int_0^t [\boldsymbol{K}(t-\tau)]\{\dot{\xi}(\tau)\}d\tau - [\boldsymbol{C}]\{\xi(t)\} + \{F^{Wind}(t)\} + \{F^{Wave}(t)\} + \{F^{Mooring}(t)\} + \{F^{Viscous}(t)\}\right\}, \tag{10}$$

where a letter in bold represents a matrix, and $\{\cdot\}$ represents a vector. The solutions at each time step can be found via the fourth-order Runge-Kutta scheme as the following

$$\{\xi(t+\Delta t)\} = \{\xi(t)\} + \Delta t \cdot \{\dot{\xi}(t)\} + \Delta t \cdot (Q_1 + Q_2 + Q_3)/6\,, \tag{11}$$

$$\{\dot{\xi}(t+\Delta t)\} = \{\dot{\xi}(t)\} + (Q_1 + 2Q_2 + 2Q_3 + Q_4)/6\,, \tag{12}$$

where

$$Q_1 = \Delta t \cdot Q\left[t, \{\xi(t)\}, \{\dot{\xi}(t)\}\right], \tag{13}$$

$$Q_2 = \Delta t \cdot Q\left[t + \Delta t/2\,, \{\xi(t)\} + \Delta t \cdot \{\dot{\xi}(t)\}/2\,, \{\dot{\xi}(t)\} + Q_1/2\right], \tag{14}$$

$$Q_3 = \Delta t \cdot Q\left[t + \Delta t/2\,, \{\xi(t)\} + \Delta t \cdot \{\dot{\xi}(t)\}/2 + \Delta t \cdot Q_1/4\,, \{\dot{\xi}(t)\} + Q_2/2\right], \tag{15}$$

$$Q_4 = \Delta t \cdot Q\left[t + \Delta t, \{\xi(t)\} + \Delta t \cdot \{\dot{\xi}(t)\} + \Delta t \cdot Q_2/2\,, \{\dot{\xi}(t)\} + Q_3\right]. \tag{16}$$

4. A Morison-Stick Method for Modeling Floating Truss Structures in Time Domain

4.1. Theory, Formulation and Numerical Implementation of the Morison-Stick Method

The viscous effect plays an important role in the dynamic response of such a semi-submersible since the diameters of the slender braces are small in comparison to the wavelengths in a typical sea condition. A Morison-type method is necessary to be employed in combination with the potential flow theory. Based on the conclusion of Liu et al. (2016), an appropriate hybrid approach can apply a Morison method in the calculation of the wave drag force and a potential flow theory-based method in the calculation of the platform inertia force. Such a combination can lead to the high accuracy of prediction. This concept will be applied as well to the present time-domain method.

Following Leblanc et al. (1993), the wave drag force upon a cylindrical member can be obtained via the integration along its length, i.e.,

$$\vec{F}_D = \frac{1}{2}\rho C_D \int_s^e D_{mem} V_{rT} \vec{V}_{rT} dl\,, \tag{17}$$

where C_D, D_{mem} and l are respectively the drag coefficient, the diameter and the length of a cylindrical member, ρ is the water density, V_{rT} is the absolute value of $\vec{V}_{rT}$ which is the transverse component of the wave-body relative velocity $\vec{V}_r$. Besides, "s" and "e" represent the start and the end of a cylindrical member, respectively. The wave-body relative velocity $\vec{V}_r$ is the difference between the wave-particle velocity $\vec{V}_w$ and the motion velocity of a floating structure $\vec{V}_m$, i.e.,

$$\vec{V}_r = \vec{V}_w - \vec{V}_m. \tag{18}$$

It is easy to know, the floating structure motion at the centroid of a Morison element can be calculated as

$$\vec{V}_m = \left(\dot{\xi}_1, \dot{\xi}_2, \dot{\xi}_3\right)^t + \left(\dot{\xi}_4, \dot{\xi}_5, \dot{\xi}_6\right)^t \times \vec{R} = \boldsymbol{P}\vec{V}_g \tag{19}$$

where $\dot{\xi}_i$ $(i = 1\sim6)$ represents the platform motion velocity in the ith DoF, $\vec{R} = \left(x - x_g, y - y_g, z - z_g\right)^t$ represents the position vector of the Morison element in the body-fixed system (the superscript "t" means "transpose" of the vector), $\vec{V}_g = \left(\dot{\xi}_1, \dot{\xi}_2, \dot{\xi}_3, \dot{\xi}_4, \dot{\xi}_5, \dot{\xi}_6\right)^t$ is the platform velocity vector at the gravity center of the floating structure, and $\boldsymbol{P}$ stands for the following translational-to-rotational transformation matrix

$$\boldsymbol{P} = \begin{bmatrix} 1 & 0 & 0 & 0 & z - z_g & -(y - y_g) \\ 0 & 1 & 0 & -(z - z_g) & 0 & x - x_g \\ 0 & 0 & 1 & y - y_g & -(x - x_g) & 0 \end{bmatrix}. \tag{20}$$

Based on the principle of the double vector product, the transverse component $\vec{V}_T$ of a velocity vector $\vec{V}$ can be expressed by

$$\vec{V}_T = \vec{l} \times \vec{V} \times \vec{l} = \vec{V} - \left(\vec{V} \cdot \vec{l}\right)\vec{l} = \boldsymbol{T}\vec{V} \tag{21}$$

where $\vec{l} = \left(l_x, l_y, l_z\right)$ is the unit vector along the axial direction of the cylindrical member to which the Morison element belongs, and $\boldsymbol{T}$ is the axial-to-transverse transformation matrix that is calculated by

$$\boldsymbol{T} = \boldsymbol{I} - \vec{l}\vec{l}^t = \begin{bmatrix} 1 - l_x^2 & -l_x l_y & -l_x l_z \\ -l_y l_x & 1 - l_y^2 & -l_y l_z \\ -l_z l_x & -l_z l_y & 1 - l_z^2 \end{bmatrix}, \tag{22}$$

where $\boldsymbol{I}$ stands for the 3-order Identity Matrix. Taking into consideration simultaneously Eqs. (18) ~ (22), the transverse component of the relative water velocity can be expressed by

$$\vec{V}_{rT} = \boldsymbol{T}\vec{V}_w - \boldsymbol{T}\boldsymbol{P}\vec{V}_g, \tag{23}$$

and the wave drag force upon a segment of a cylindrical member can be written as

$$\vec{F}_D^{i,j} = \frac{1}{2}\rho C_D^i D_{mem}^i (\delta l)^{i,j} \left|T^{i,j}\vec{V}_w^{i,j} - T^{i,j}P^{i,j}\vec{V}_g\right| \left(T^{i,j}\vec{V}_w^{i,j} - T^{i,j}P^{i,j}\vec{V}_g\right), \tag{24}$$

$$\vec{M}_D^{i,j} = \vec{R}^{i,j} \times \frac{1}{2}\rho C_D^i D_{mem}^i (\delta l)^{i,j} \left|T^{i,j}\vec{V}_w^{i,j} - T^{i,j}P^{i,j}\vec{V}_g\right|\left(T^{i,j}\vec{V}_w^{i,j} - T^{i,j}P^{i,j}\vec{V}_g\right). \quad (25)$$

where the superscripts '*i*, *j*' stand for the *j*th Morison segment of the *i*th cylindrical member. Therefore, the viscous force at the right-hand side of Eq. (1) can be finally deduced in the following form

$$\vec{F}^{Viscous}(t) = \sum_{i=1}^{N_{mem}} \sum_{j=1}^{N_{seg}^i} (P^{i,j})^t \times \vec{F}_D^{i,j}. \quad (26)$$

where N_{mem} represents the number of all cylindrical members and N_{seg}^i represents the number of Morison segments on the *i*th cylindrical member. Upon each tubular member, the local incident wave kinematics, as mentioned in Section 4.2, is used to calculate its quadratic wave drag force in either a regular wave or irregular waves by the Morison dynamic solver. The vector $\vec{F}^{Viscous}$ is then calculated at every time step with the present displacement and the motion velocity of the floating structure. Thereafter, by resolving the time domain motion equation Eq. (10), the displacement and the motion velocity of the floating structure can be updated for the calculation at the next time step.

In respect of the numerical implementation of the wave drag model, a Morison-stick mesh generator is specially developed to generate the stick mesh. As shown in Figure 3, the hybrid mesh is created for the immersed part of the floating structure under the mean water level. The number of Morison segments on each of the cylindrical members can be set at the users' discretion in advance. In the stick-mesh generator, the location and affiliation of each Morison segment on each of the cylindrical members, the equivalent cross-section diameter, the axis length, the axis direction, and the drag coefficients C_D of each cylindrical member, are recorded into the generated stick mesh as an input file to the time-domain solver.

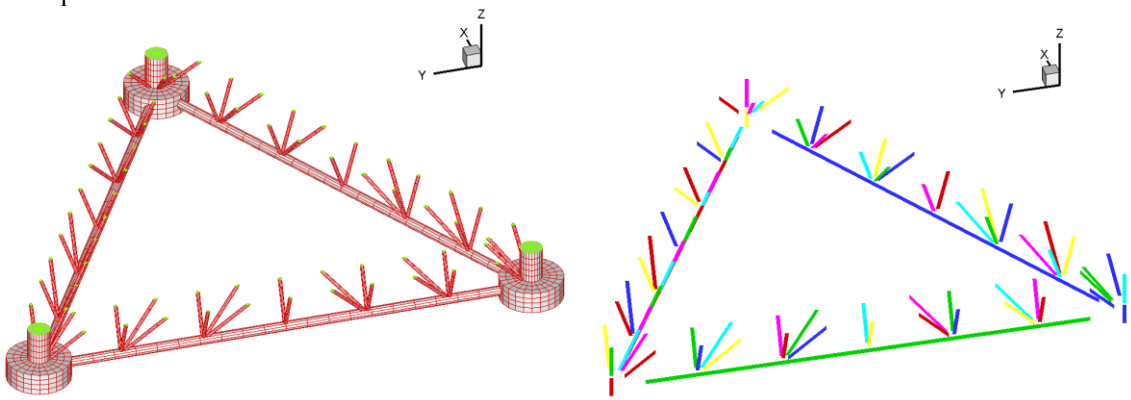

Figure 3. A hybrid panel-stick model for the floating truss structure: (a) a panel mesh for calculation of the wave inertia forces using the potential flow method; (2) a stick mesh for calculation of the wave drag force using the Morison method.

4.2. Fluid Kinematics of Incident Waves in Regular and Irregular Waves

Considering an Airy wave transmitting with a small amplitude A and an angular frequency w, in the water with a finite depth of h, the incident wave potential for this regular wave at any position (x,y,z) can be described by

$$\Phi(x,y,z,t) = \mathrm{Re}\left[-\frac{\mathrm{i}gA}{\omega}\frac{\cosh k(z+h)}{\cosh kh} e^{\mathrm{i}k(x\cos\beta + y\sin\beta) - \mathrm{i}\omega t}\right], \quad (27)$$

where β is the wave heading angle measured from the positive x-direction, and k is the wavenumber. By taking the derivative with respect to time t, the wave-particle velocity in the space can be deduced as

$$U(x,y,z,t) = \frac{\partial\Phi}{\partial x} = \frac{gkA\cos\beta}{\omega}\frac{\cosh k(z+h)}{\cosh kh}\cos[k(x\cos\beta + y\sin\beta) - \omega t], \quad (28)$$

$$V(x,y,z,t)=\frac{\partial\Phi}{\partial y}=\frac{gkA\sin\beta}{\omega}\frac{\cosh k(z+h)}{\cosh kh}\cos[k(x\cos\beta+y\sin\beta)-\omega t], \tag{29}$$

$$W(x,y,z,t)=\frac{\partial\Phi}{\partial z}=\frac{gkA}{\omega}\frac{\sinh k(z+h)}{\cosh kh}\sin[k(x\cos\beta+y\sin\beta)-\omega t], \tag{30}$$

where U, V, and W represent the fluid velocity $\vec{V}_w$ in x, y, and z-direction, respectively. In irregular waves, the above three components can be finally derived as

$$U(x,y,z,t)=\sum_{i=1}^{N}\frac{gk_iA_i\cos\beta}{\omega_i}\frac{\cosh k_i(z+h)}{\cosh k_ih}\cos[k_i(x\cos\beta+y\sin\beta)-\omega_it+\varepsilon_i], \tag{31}$$

$$V(x,y,z,t)=\sum_{i=1}^{N}\frac{gk_iA_i\sin\beta}{\omega_i}\frac{\cosh k_i(z+h)}{\cosh k_ih}\cos[k_i(x\cos\beta+y\sin\beta)-\omega_it+\varepsilon_i], \tag{32}$$

$$W(x,y,z,t)=\sum_{i=1}^{N}\frac{gk_iA_i}{\omega_i}\frac{\sinh k_i(z+h)}{\cosh k_ih}\sin[k_i(x\cos\beta+y\sin\beta)-\omega_it+\varepsilon_i], \tag{33}$$

where the subscript i represents the ith frequency component, ε_i is a random phase uniformly distributed between 0 and 2π. The ith component of wave amplitude A_i can be calculated from

$$A_i(\omega_i)=\sqrt{2S(\omega_i)\Delta\omega_i}, \tag{34}$$

where $\Delta\omega_i$ is the bandwidth of the discretized wave angular frequency, and $S(\omega_i)$ represents the local power spectrum of irregular waves at a specific site, e.g., JONSWAP (Joint North Sea Wave Observation Project) spectrum, P-M (Pierson-Moskowitz) spectrum, etc. Note that for the deepwater case, the ratio of two hyperbolic functions degrades to the exponential function e^{kz} in Eqs. (27) ~ (30) and e^{k_iz} in Eqs. (31) ~ (33).

5. Validation of the Time-Domain Hybrid Panel-Stick Method

A model experiment was carried out in the towing tank (65m length, 5m width, and 7m depth) of RIAM, Kyushu University. The purpose of the experiment was to check the hydrodynamic performance of the platform and provide a benchmark database for the validation of the numerical code. The platform test model was of 1/50 scale, with a displacement of 0.01693 m^3. Each catenary mooring line in the model experiment was substituted by a spring that had an equivalent stiffness to the linearized stiffness of the mooring line. All the springs were anchored to a movable steel frame, which was specifically set for the arrangement of the mooring layout (Figure 4). Two high-speed digital cameras (DITECT HAS-L1™, 1280×1024 pixel, 50fps) are set aside the towing tank, and three yellow spherical markers are set atop the rotor plate for the motion capturing during the experiment.

Before the tank test, the camera system was calibrated by a cubic steel frame with eight spherical markers respectively set at its vertices. The positions of the eight markers in the user-defined coordinate system and two photos of the cubic steel frame from the respective view of each camera were input to the DippMotionPro3D ™ software that was used for processing the camera-recorded videos. When the tank test started, the wind and the waves could be generated and therefore caused the floating platform to oscillate. The platform motion was captured via the movements of the three markers, respectively, by the two monitoring cameras. After the completion of the tank test, the DippMotionPro3D ™ software was used to analyze the videos and calculate the motion time histories of the three markers. Thereby, any point on the floating platform could be calculated based on its relative position to the three markers.

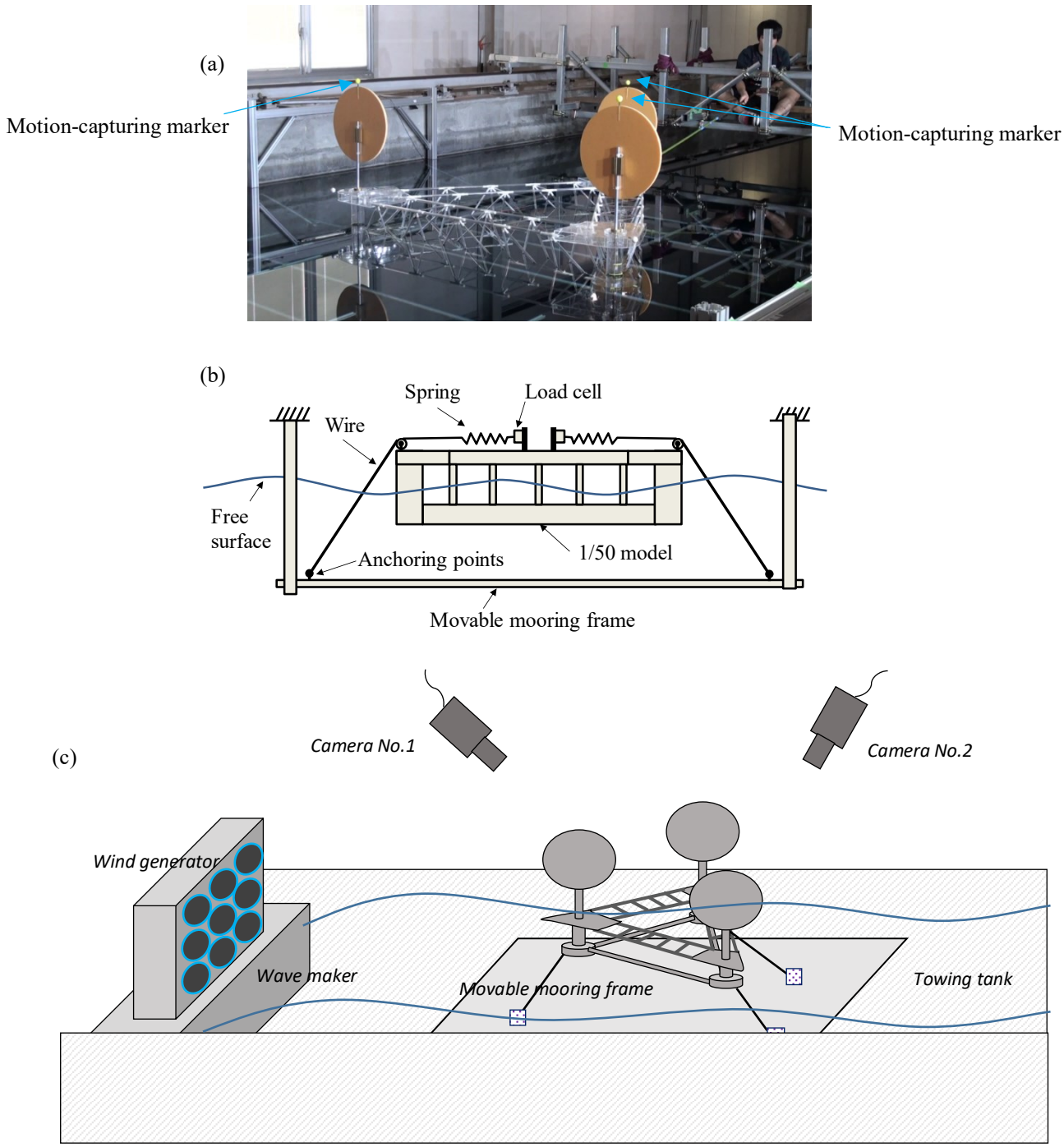

Figure 4. (a) Photo of the experimental model; and a sketch of the experimental setup: (b) tank cross-sectional view, (c) side view.

To validate the preceding hybrid panel-stick time-domain method, the wind was not taken into consideration in either the experiment or the numerical model. The experimental conditions of incident regular waves are given in Table 3. In the numerical model, the wavelengths of the incident regular waves range from 0.05L to 7.0L (L is the characteristic length of the triangular platform), and the time step is T/100 (T is the wave period). The numerical results of the present time-domain method are compared with the frequency-domain results as well as the experimental in Figure 5 and Figure 6. For the fairness between the numerical models, in the frequency-domain model, only the incident waves are considered for the wave kinematics in order to be consistent with Eqs. (27)~(30) of the time-domain model. This means that the wave field is considered not to have been disturbed

by the diffracted waves. In general, good agreements can be found between the simulation results and the experiment data. However, an exception occurs in the heave motion that the experimental data are a bit lower than the numerical simulations (when $\lambda/L > 5.0$), while the latter two tend to approach unity with the increase of λ/L. Newman (1999) proved theoretically that in the long-wavelength regime, the heave RAO should approach unity, which in general agrees with the numerical results in Figure 5(b) and Figure 6(c). Moreover, the discrepancies between the frequency-domain and the time-domain results for the heave motion prove the sensitivity of numerical models within this resonant region. When wave heading is 90 deg, the platform is mainly excited in the sway direction. Therefore the motion RAO in surge is small, and the respective measuring error using the experimental facility is larger, which is acceptable and within expectation.

Table 3 Experimental conditions of incident regular waves

Wave Period (sec)	Wave Length (m)	Wave Height (cm)	Ratio λ/L
0.71	0.78	1.56	0.5
0.89	1.25	2.50	0.8
1.00	1.56	3.12	1.0
1.10	1.87	3.74	1.2
1.22	2.34	4.68	1.5
1.30	2.65	5.30	1.7
1.41	3.12	6.24	2.0
1.73	4.67	4.68	3.0
2.00	6.24	6.24	4.0
2.12	7.02	7.02	4.5

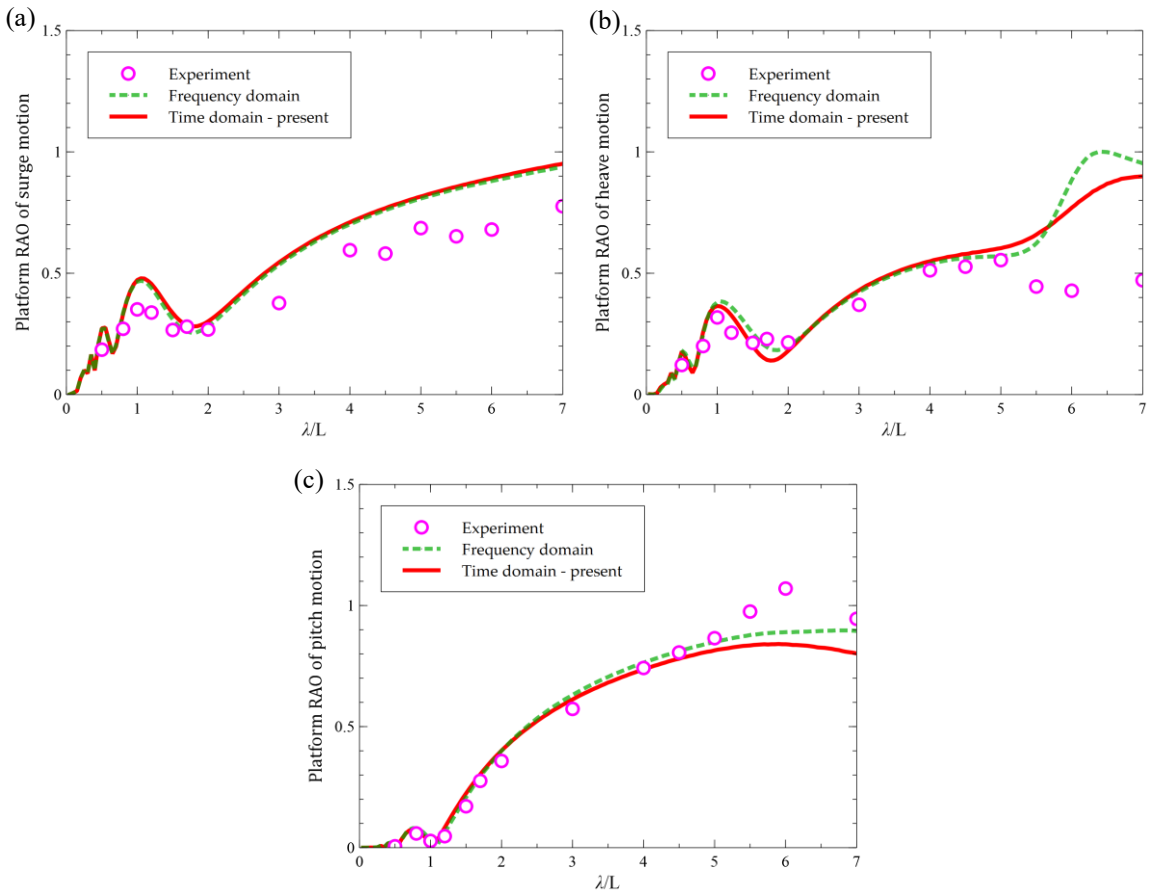

Figure 5. Comparison of the present time-domain method and the model experiment in a regular wave with a heading angle $\beta = 0$ deg: (a) platform surge RAO; (b) heave RAO; (c) pitch RAO. No wind has been considered in either of the numerical model or the experiment model.

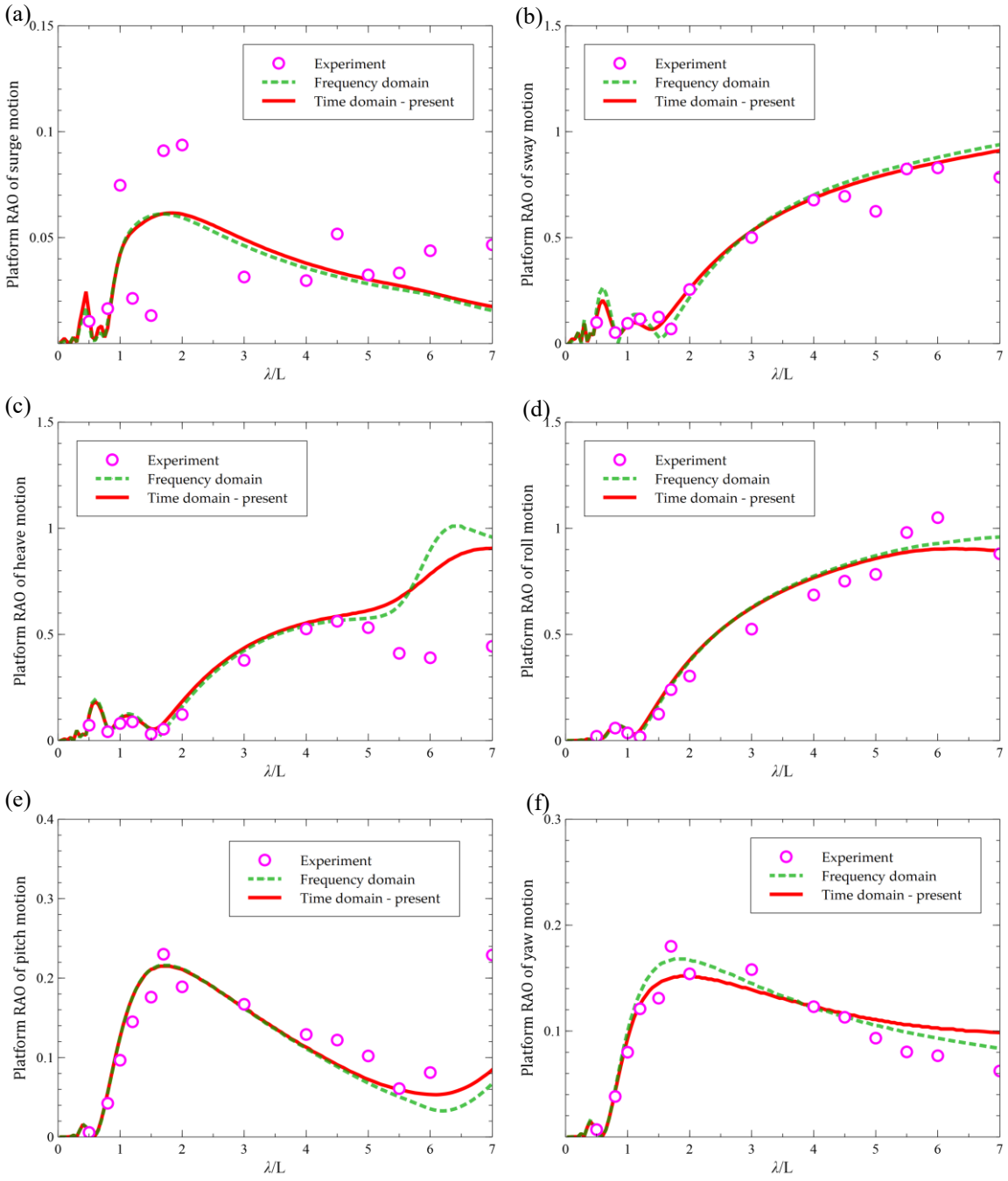

Figure 6. Comparison of the present time-domain method and the model experiment in a regular wave with a heading angle $\beta = 90$ deg: (a) platform surge RAO; (b) sway RAO; (c) heave RAO; (d) roll RAO; (e) pitch RAO; (f) yaw RAO. No wind has been considered in either of the numerical model or the experiment model.

6. Results and Discussion

6.1. Load Cases of the Simulations

In order to analyze the effect of the wave drag force on the motion response of the FWT with numerous truss members, numerical simulations are thereby performed based on the developed time-domain method. Simulations for the FWT in parked status and operating status are carried out

separately to discover different phenomenon and reveal different mechanisms. The load cases are shown in Table 4 for the subsequent analysis. For the wind conditions, wind speeds at the rated case (V_{wind} = 11.4 m/s) and an above-rated case (V_{wind} = 15.2 m/s) have been considered. At the above-rated case, the wind turbine applies a collective blade pitch controller. In respect of the wave conditions, unidirectional irregular waves with spectrums in JONSWAP type are considered. As shown in Figure 7, simulated spectrums are evaluated from the simulated wave dynamics based on Eq. (27), which are found to be in good agreement with the theoretical spectrums. In addition, for the convenience of the analysis, natural frequencies of the FWT system can be evaluated beforehand with the assist of Hydrostar™ (Chen, 2001) or HAMS© (Liu, 2019), an open-source software package MAP++© (Masciola et al., 2013a, 2013b) and its python wrapper (Masciola, 2015; Liu et al., 2018b), which are listed in Table 5. Based on a heave free decay test performed by CFD in OpenFOAM©, the heave natural period can be calculated from Figure 8 as 17.44 s, which is very much close to the heave natural period from the present method, i.e., 2π/0.36=17.45 s.

Table 4. Load cases in the subsequent simulations.

Wave/Wind Direction	Wave Conditions		Wind and Rotor Conditions		
	H_s	T_p	V_{wind}	Rotation Speed	Blade Pitch
0 deg	2.44 m	8.10 s	0.0 m/s	0.0 rpm	0.0 deg
			15.2 m/s	12.0 rpm	10.0 deg
90 deg	1.40 m	6.50 s	0.0 m/s	0.0 rpm	0.0 deg
			11.4 m/s	12.0 rpm	0.0 deg

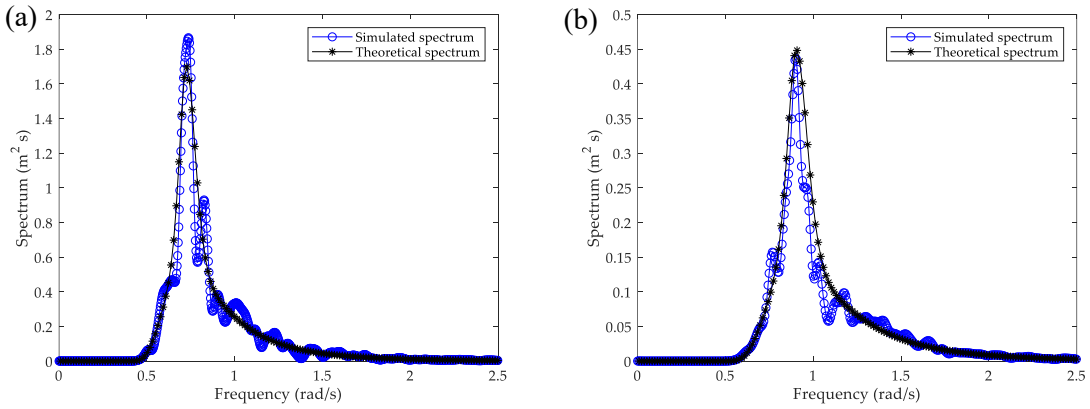

Figure 7. Wave spectrums of unidirectional irregular waves in the simulation. The spectrums are JONSWAP type with a peak enhancement factor γ= 3.3. Left: significant wave height H_s = 2.44 m, peak wave period T_p = 8.1 s; right: significant wave height H_s = 1.4 m, peak wave period T_p = 6.5 s.

Table 5. Natural frequencies of the FWT system with and without mooring.

Mode	Natural frequencies (rad/s)	
	without mooring	with mooring
Surge	-	0.07
Sway	-	0.07
Heave	0.36	0.36
Roll	0.31	0.32
Pitch	0.32	0.32
Yaw	-	0.09

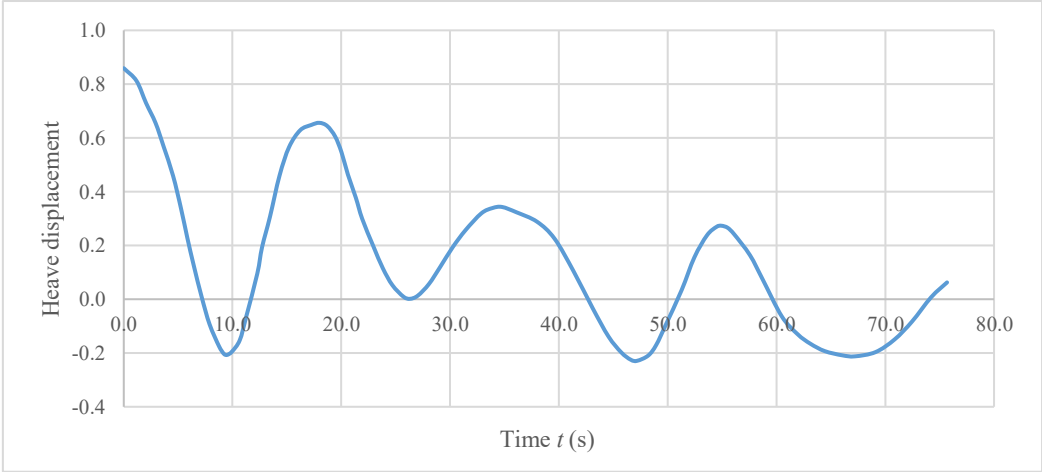

Figure 8. Free decay test simulated by CFD in OpenFOAM©.

6.2. Motion Response of the Floating Wind Turbine in Parked Status

Since the wave drag force (acting as a certain kind of viscous wave damping) upon an FWT platform is purely hydrodynamic, priority is first given to the motion response of the proposed FWT when it is in parked conditions. There is no wind (in still air) but only waves. For simplicity, misalignment between waves and wind has not been considered, i.e., waves and wind always inflow from the same direction. Responses of the FWT system are simulated using the aforementioned time-domain method. Before the numerical simulation, a convergence test is performed against the time step, as shown in Figure 9. It is found that the size of the time step has little influence on the time-history results. Therefore, a time-step of 0.5 seconds is chosen for each simulation, with a simulation time of 2048 seconds (2 to the power of n, n is an integer) for the sake of the subsequent spectral analysis using FFT (Fast Fourier Transform method). Time series of the platform motions in 6-DOF modes are shown in Figures 10 and 11, respectively, for the wind/wave directions in 0 deg and 90 deg.

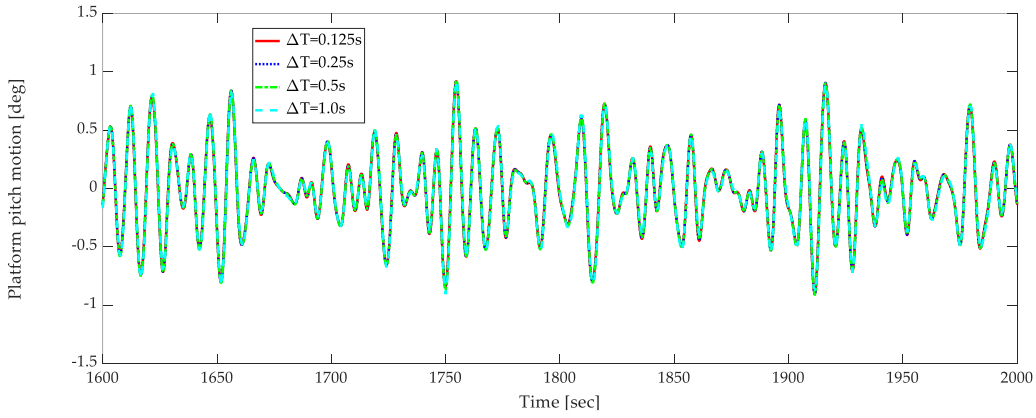

Figure 9. Convergence test with respect to the time step in the numerical simulations.

As shown in Figure 10, since the waves incident from 0 deg (toward the positive x-direction), the platform basically displaces in surge, heave, and pitch modes. Figure 10(a), (e), and (i) (particularly (e), and (i)) show that the amplitude of the platform motion response is decreased due to the existence of the viscous effect. The averaged response amplitudes of heave and pitch motions are significantly decreased by respectively 57.85% and 13.92%. Also, with the inclusion of the fluid viscosity, the coupling between different motion DoFs is likely to be enhanced, as can be observed from Figure 10(g) and (k). Based on the 'dat2spec' subroutine of the WAFO© (Wave Analysis for Fatigue and Oceanography) open-source toolbox (Brodtkorb et al., 2000), spectral analysis is performed on the motion response time series in each mode. It is seen that in surge, heave, and pitch, a pure potential flow model without any viscosity leads to a resonant response in correspondence to

404 the natural frequency of the FWT system in that mode. While applying a hybrid panel-stick model
405 can be effective to include the fluid viscosity and hence reduce the fictitious energy of the resonant
406 response. Figure 10(b), (f), and (j) show that the surge, the heave, and the pitch resonances occur at
407 respectively ω = 0.0644 rad/s, ω = 0.3528 rad/s, and ω = 0.2761 rad/s, which are close to respectively
408 the surge natural frequency ω = 0.07 rad/s, the heave natural frequency ω = 0.36 rad/s, and the pitch
409 natural frequency ω = 0.32 rad/s, as displayed in Table 5. Moreover, Figure 10(e) and 6 (i) show that
410 the wave drag force reduces the mean amplitude of the motion time series in heave and pitch,
411 respectively. In addition to the resonant responses, there exists another wave-induced response that
412 is excited by the irregular waves, the peak frequency of which corresponding to the peak frequency
413 of the incident wave spectrum. Figure 10(b), (f), and (j) show that the wave drag force slightly reduces
414 the peak of the wave-induced response. Since the wave incidents from 0 deg, the sway, the roll, and
415 the yaw motions are reasonably in extremely small magnitudes. In Figure 10(g), the existence of
416 viscous damping likely increases the magnitude of the roll motion. That is because, without viscous
417 damping, the roll motion should be almost zero. In contrast, with the existence of viscous damping,
418 which can be viewed as an equivalent to a damping matrix, the roll motion is slightly disturbed by
419 the motions in other modes such as heave, etc. However, since the values are almost negligible, it is
420 hard to draw significant conclusions based on these limited results and, therefore, should be
421 considered further.
422

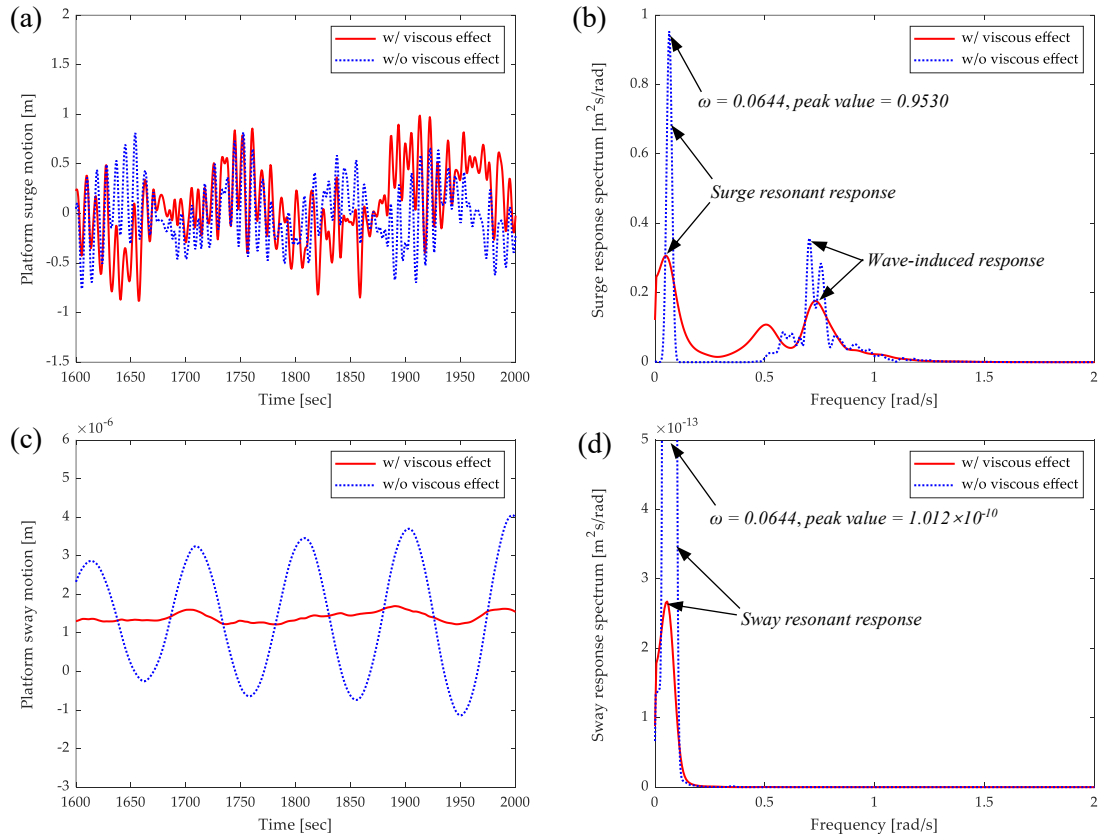

423
424

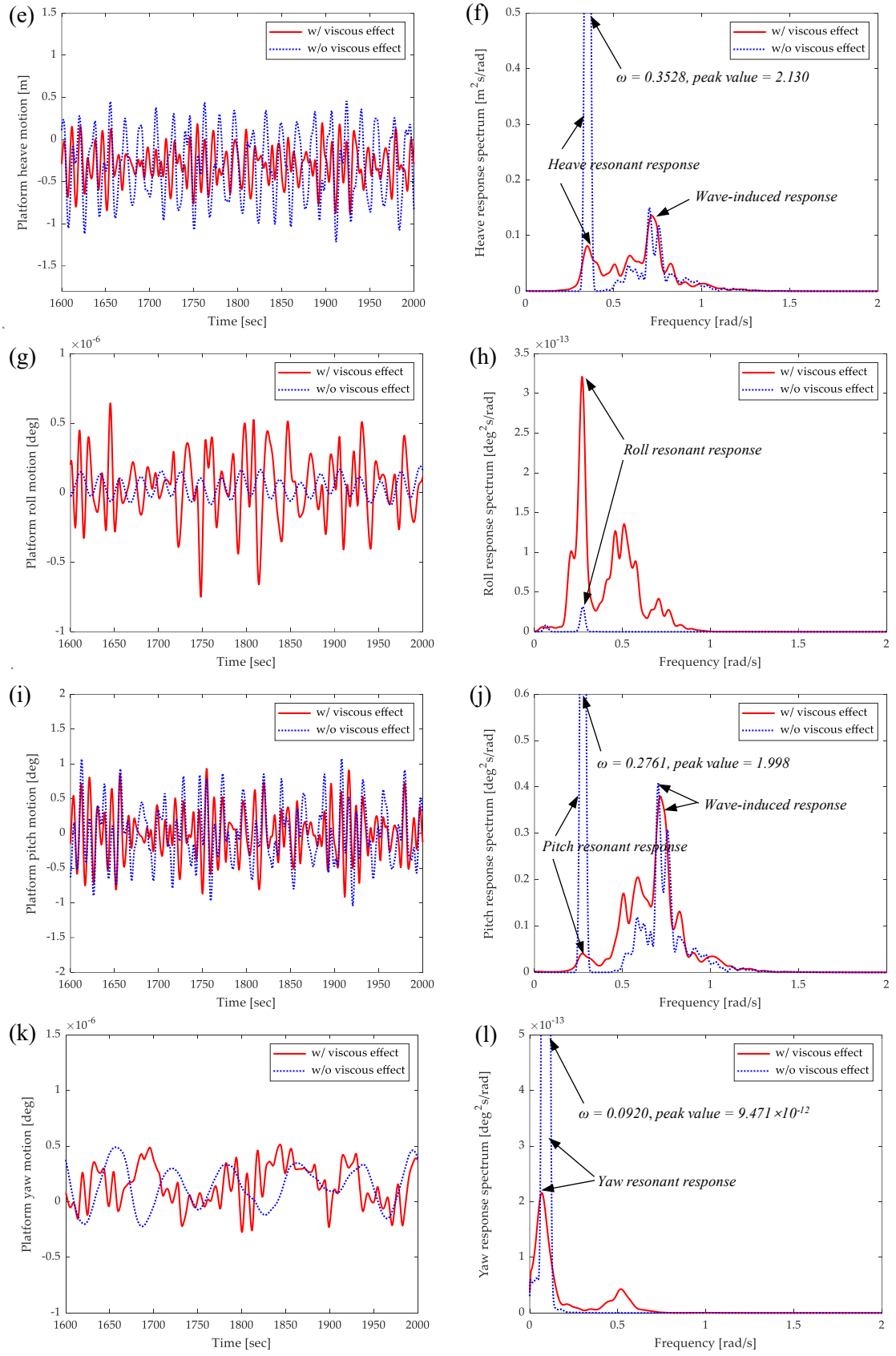

Figure 10. Time history of the FWT and the spectral analysis. The environmental conditions in the numerical model: no wind (wind speed V_{wind} = 0 m/s); unidirectional irregular waves (significant wave height H_s = 2.44 m, peak wave period T_p = 8.1 s, wave heading angle β = 0 deg).

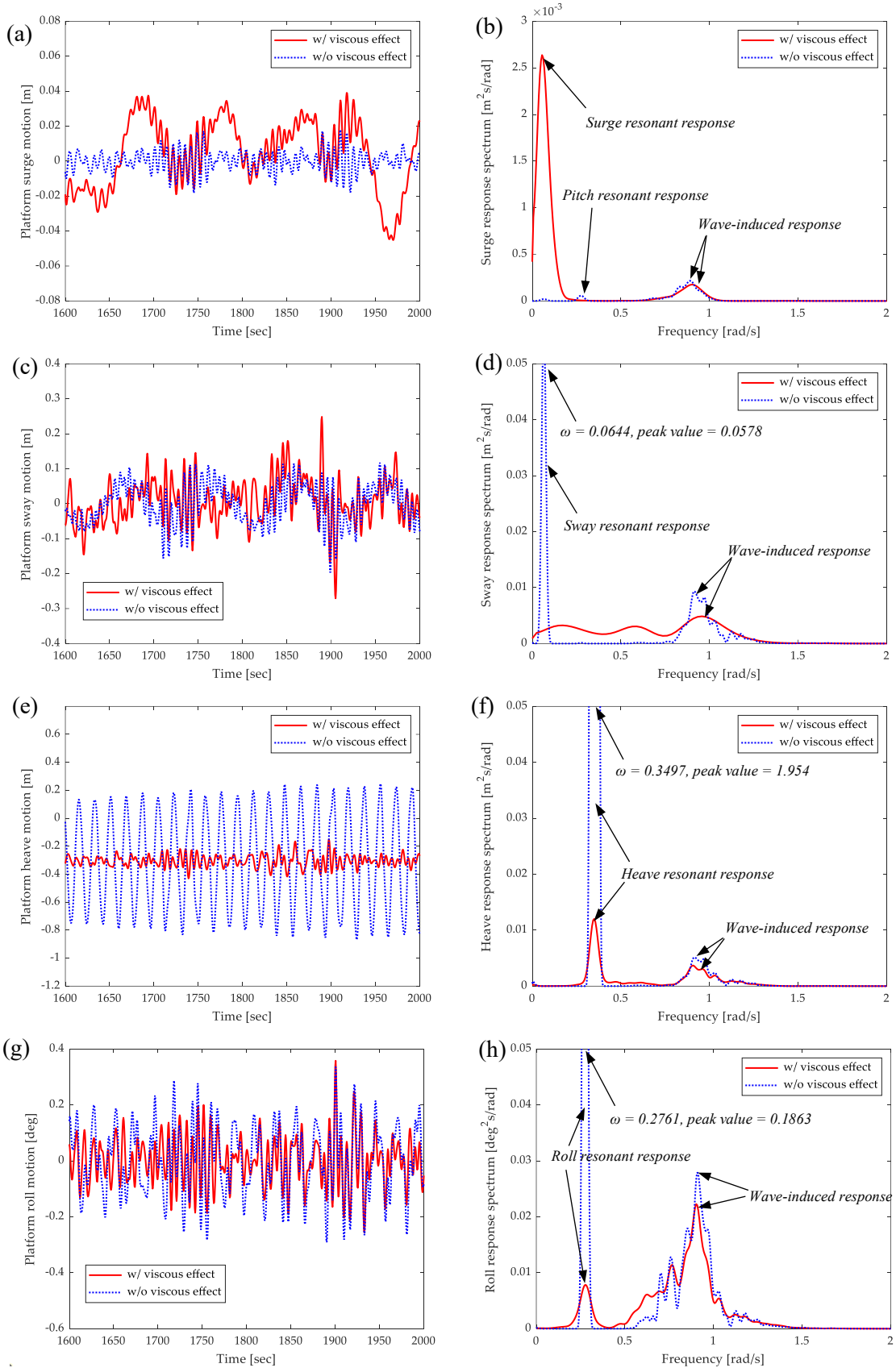
(a)
w/ viscous effect
w/o viscous effect
Platform surge motion [m]
Time [sec]
(b)
×10^-3
Surge response spectrum [m^2s/rad]
Surge resonant response
Pitch resonant response
Wave-induced response
Frequency [rad/s]
(c)
Platform sway motion [m]
Time [sec]
(d)
Sway response spectrum [m^2s/rad]
ω = 0.0644, peak value = 0.0578
Sway resonant response
Wave-induced response
Frequency [rad/s]
(e)
Platform heave motion [m]
Time [sec]
(f)
Heave response spectrum [m^2s/rad]
ω = 0.3497, peak value = 1.954
Heave resonant response
Wave-induced response
Frequency [rad/s]
(g)
Platform roll motion [deg]
Time [sec]
(h)
Roll response spectrum [deg^2s/rad]
ω = 0.2761, peak value = 0.1863
Roll resonant response
Wave-induced response
Frequency [rad/s]

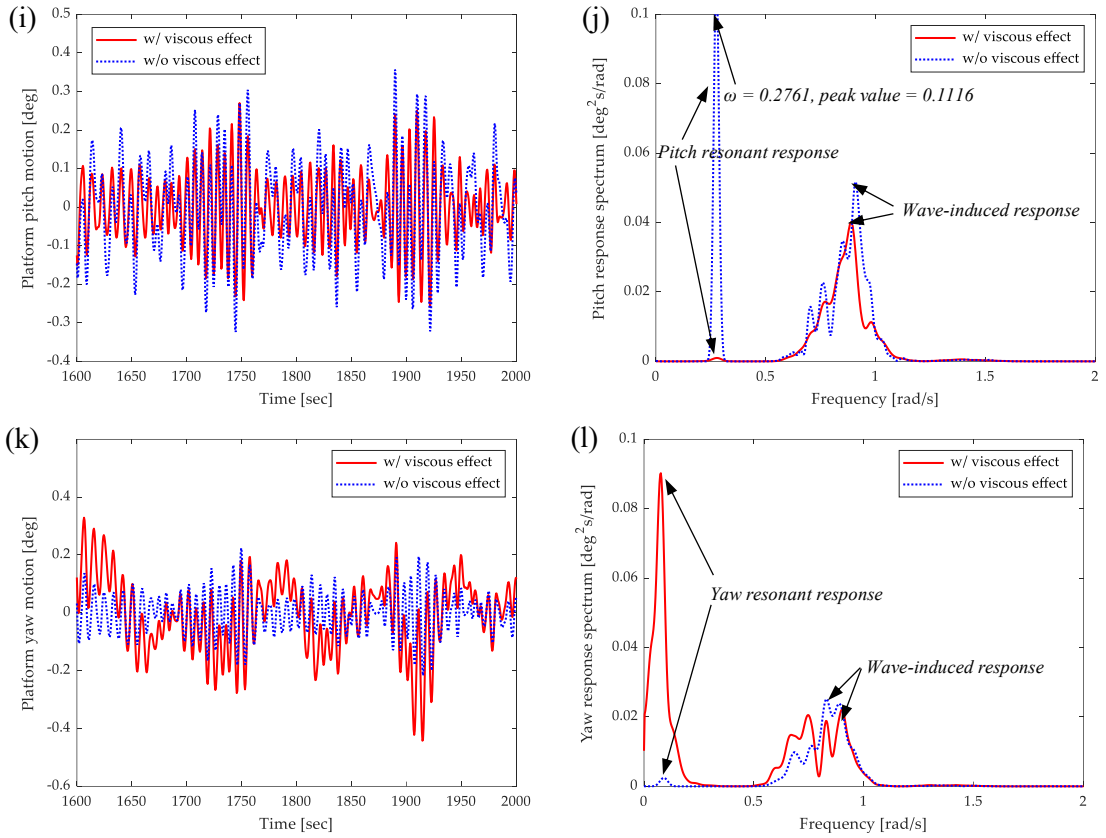

Figure 11. Time history of the FWT and the spectral analysis. The environmental conditions in the numerical model: no wind (wind speed V_{wind} = 0 m/s); unidirectional irregular waves (significant wave height H_s = 1.4 m, peak wave period T_p = 6.5 s, wave heading angle β = 90 deg).

Figure 11 shows the motion time series of the FWT when the waves incident from the 90 deg direction. The platform displaces basically in sway, heave, roll, and yaw, while the pitch motion is strongly coupled with the heave motion, as shown in Figure 11(c), (e), (g), (i) and (k). Figure 11(a) shows that the surge motion is also affected by enhancing the motion response of the resonant frequency component. Figure 11(d), (f), (h) and (j) show that the sway, the heave, the roll and the pitch resonances occur at respectively ω = 0.0644 rad/s, ω = 0.3497 rad/s, ω = 0.2761 rad/s and ω = 0.2761 rad/s, which are close to respectively the sway natural frequency ω = 0.07 rad/s, the heave natural frequency ω = 0.36 rad/s, the roll natural frequency ω = 0.32 rad/s and the pitch natural frequency ω = 0.32 rad/s, as displayed in Table 5. With the existence of the fluid viscosity, the resonances are effectively reduced, which can be known from the red-line simulation results with the wave viscous damping. Moreover, similar to that has been found in Figure 10, the viscous wave effect decreases slightly the peak of the wave-induced response excited by the irregular waves with a JONSWAP spectrum, as shown in Figure 11(d), (f), (h), (j) and (l). Worth noting is that the presence of the fluid viscosity is likely to enhance the coupling between the motions in different DoFs, which can be observed from the resonant response energy of the yaw response spectrum, as shown in Figure 11(l).

6.3. Motion Response of the Floating Wind Turbine in Operation

After knowing the motion response characteristics of the FWT in the still-air condition, it is interesting to know what the characteristics will be like if the wind is involved as well. In this section, therefore, simulations are performed for the FWT when it is in operation. To give a clear explanation, turbulent winds and misalignments between wind and waves are not considered here. In other words, the wind steadily comes from the same direction as the waves. Each of the simulations lasts

for 2048 seconds with a time step of 0.5 seconds. Time series of the platform motions in 6-DoF modes are shown in Figures 12 and 13, respectively, for the wind/wave directions in 0 deg and 90 deg.

Figure 12 shows the platform motion time histories and the spectral analysis when the waves and the wind come from the positive x-direction. Similar to Figure 10, the platform displaces in surge, heave, and pitch, as shown in Figure 12(a), (e) and (i). It is found that, in general, the motion amplitudes in almost all the DoFs have been decreased by the inclusion of the fluid viscosity in the presence of wind. Again, the same resonant frequencies are obtained with the aid of the WAFO© toolbox, which are in coincidence with the natural frequencies in Table 5. Worth noting is that the resonance in the surge motion without the fluid viscosity can be excited prominently in the presence of the wind. That is to say, the one component of the surge motion (which consists of an infinite set of components with different frequencies) with a frequency equivalent to that of the surge resonance (ω = 0.0644 rad/s) are particularly excited due to the existence of the wind. This phenomenon can be confirmed again by the spectral analysis of the pitch motion time series, as given in Figure 12(j). In comparison to Figure 10(j), i.e., the case without wind, there is an additional distinctive resonant response with a peak at the surge resonance frequency (ω = 0.0644 rad/s). It can be known for sure that this peak is induced by the resonant response of the surge motion since the pitch and the surge motions are strongly coupled. However, in the presence of the fluid viscosity, the surge resonant response diminishes, and the pitch resonant response is also significantly reduced, as shown in Figure 10(b) and 10(j).

The reason why the steady wind excites the surge resonance can be explained as below: (1) In the still-air condition, as shown in Figure 10(a), the equilibrium position of the platform motion is set at the origin of the ground-based global coordinate system. Starting from the equilibrium position, the platform moves with an initial velocity, which is induced by the waves. (2) In the presence of the steady wind, the equilibrium position of the platform surge motion changes to a place having a distance (2.5 m in the present case as shown in Figure 12(a)) from the origin, resulting from the new balance between the actions of the wind thrust force, the wave excitation force and the mooring restoring force. The work that the wind has done to the FWT along the 2.5 m distance increases the total kinetic energy of the platform remarkably and therefore increases the surge velocity of the platform at the equilibrium position. (3) Without the existence of wave viscous damping (much larger than the wave radiation damping at the platform resonant frequency), the amplitude of the platform surge motion can increase to a considerable value. In reality, the existence of wave viscous damping reduces the amplitude of the platform motion significantly.

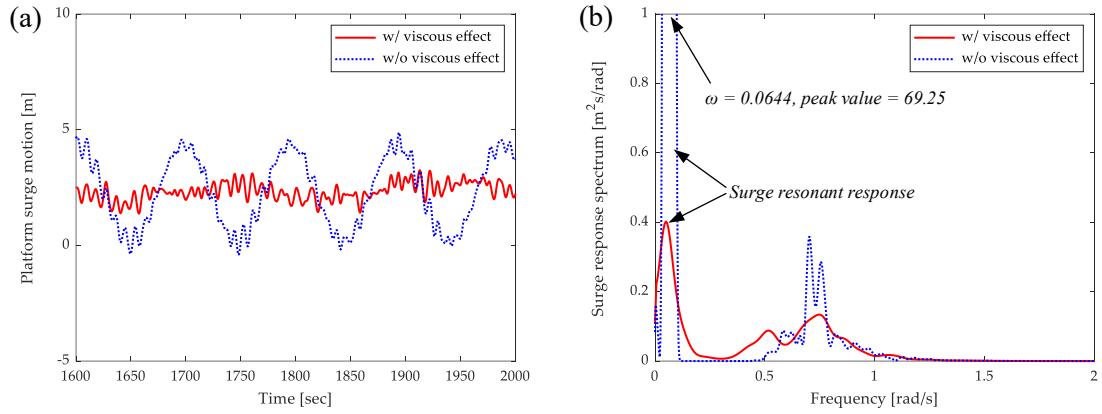

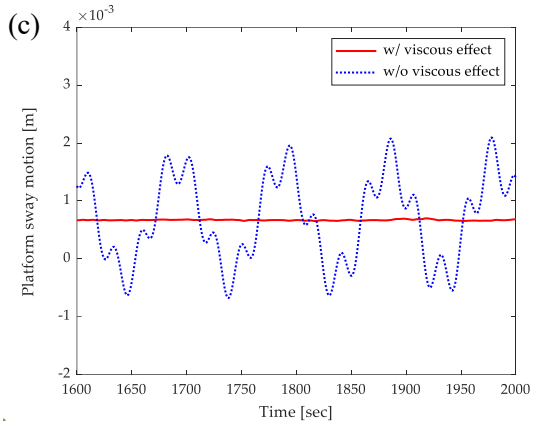

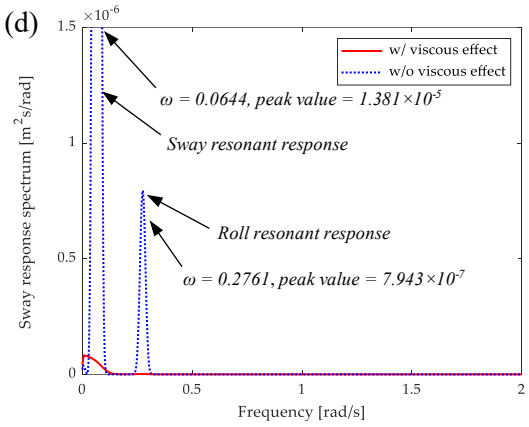

496

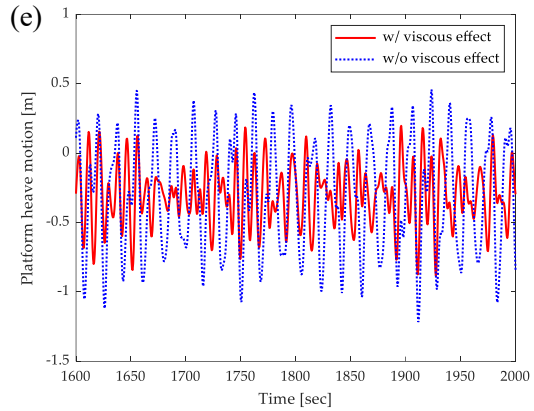

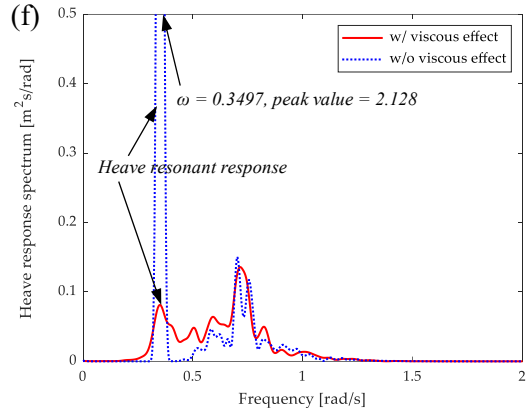

497

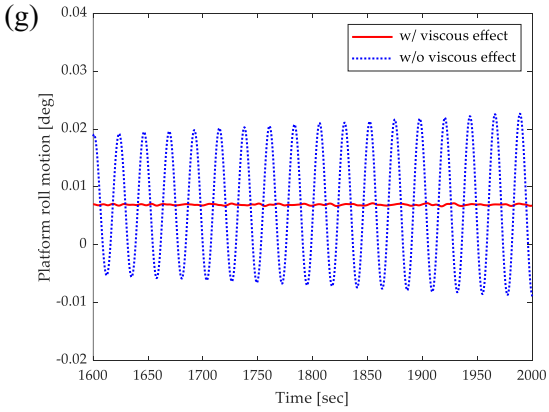

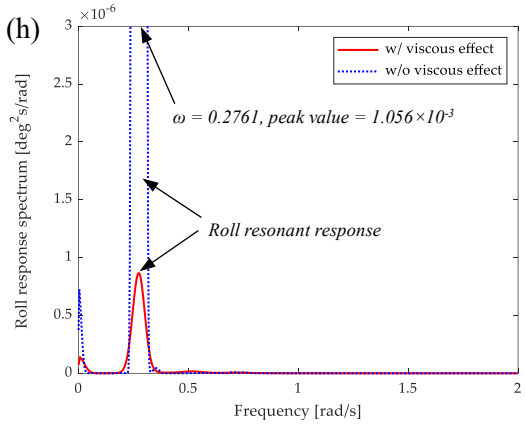

498

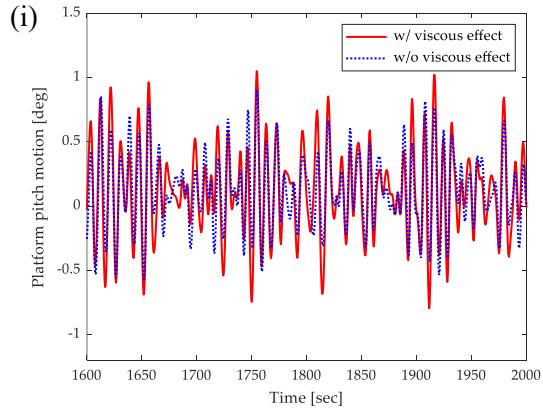

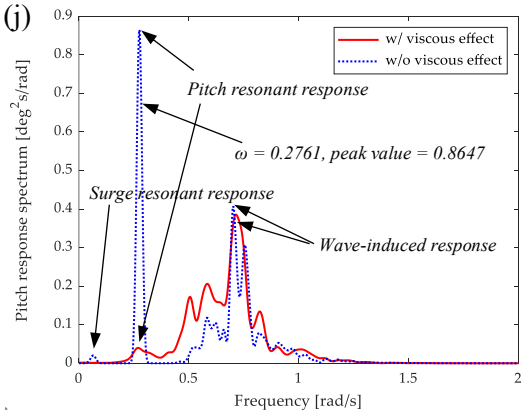

499

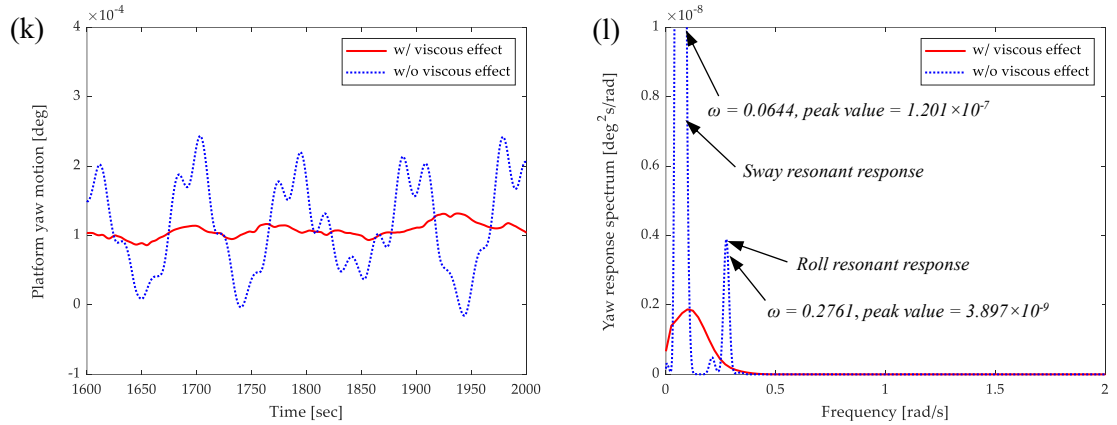

Figure 12. Time history of the FWT and the spectral analysis. The environmental conditions in the numerical model: steady wind (wind speed V_{wind} = 15.2 m/s, wind direction α = 0 deg); unidirectional irregular waves (significant wave height H_s = 2.44 m, peak wave period T_p = 8.1 s, wave heading angle β = 0 deg).

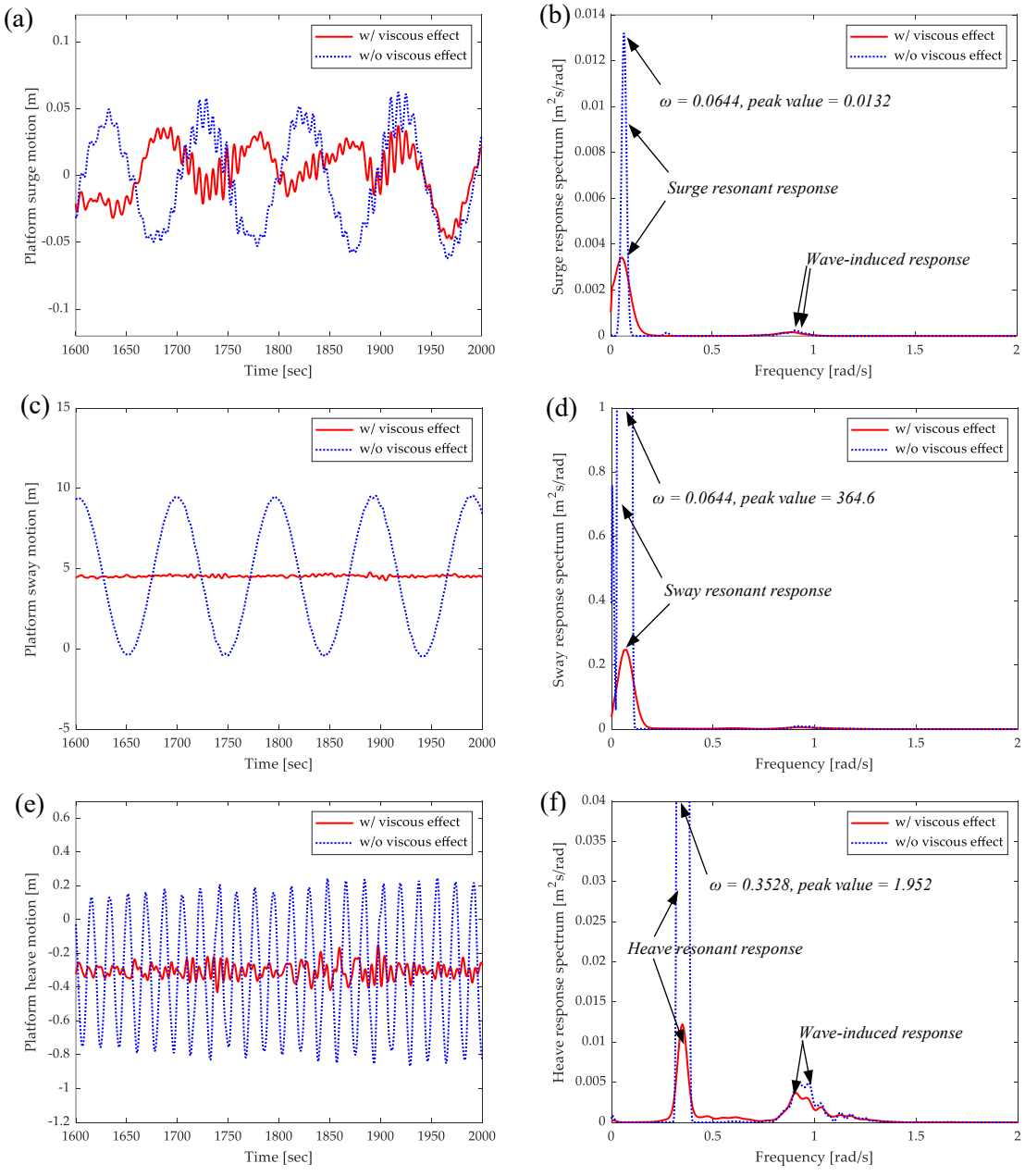

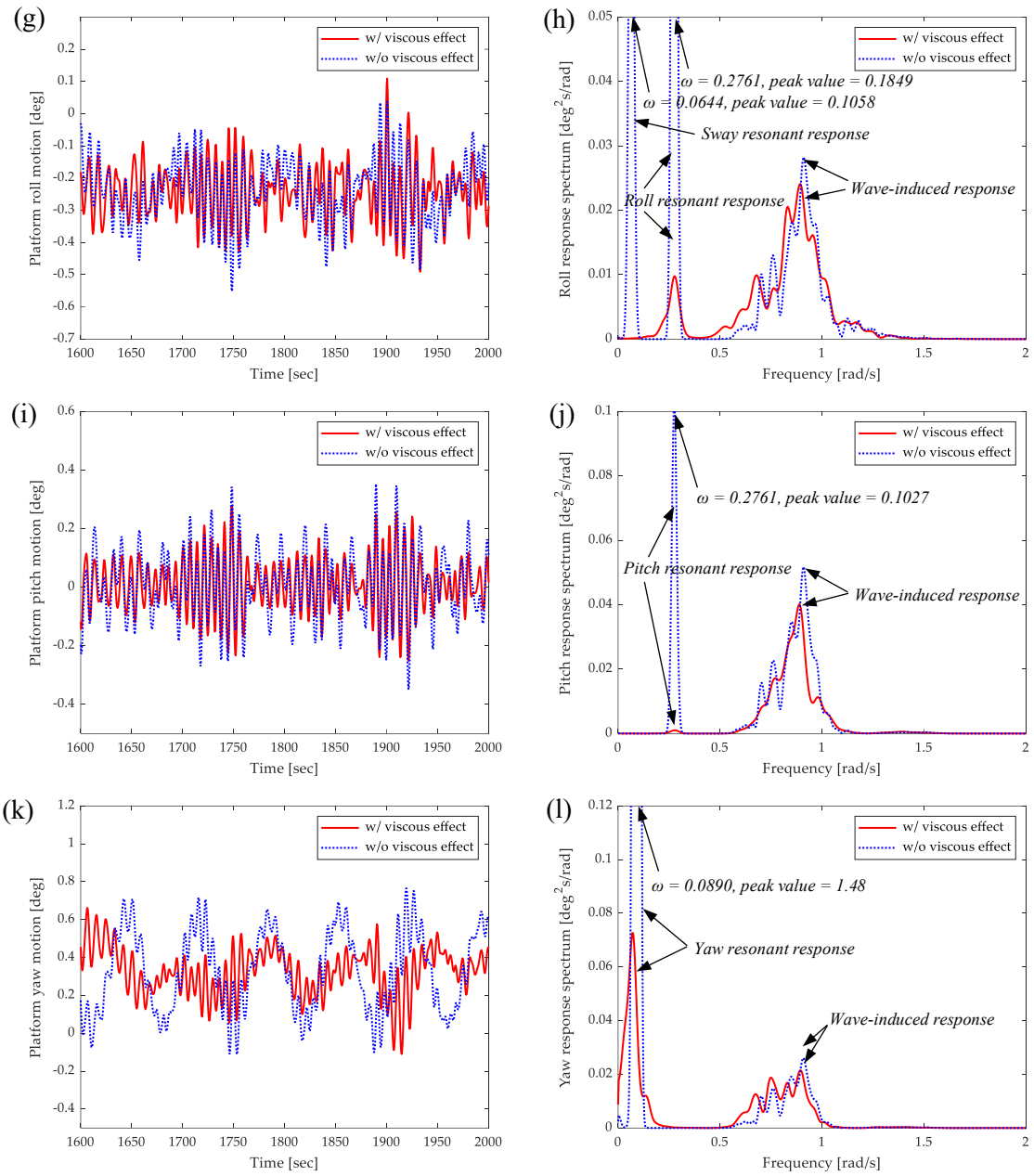

Figure 13. Time history of the FWT and the spectral analysis. The environmental conditions in the numerical model: steady wind (wind speed V_{wind} = 11.4 m/s, wind direction α = 90 deg); unidirectional irregular waves (significant wave height H_s = 1.4 m, peak wave period T_p = 6.5 s, wave heading angle β = 90 deg).

Figure 13 shows the motion time series of the FWT when the waves and the wind come from the 90 deg direction. Similar to Figure 11, the platform displaces basically in sway, heave, roll, and yaw, as well as pitch that is induced by the coupled heave motion, as shown in Figure 13(c), (e), (g), (k) and (i). Figure 13(a) shows that the surge motion is affected as well by enhancing the motion response of the resonant frequency component. Again, the translational sway motion with the assumption of no fluid viscosity is excited particularly at the sway resonant frequency (ω = 0.0644 rad/s), which is close to the natural frequency (ω = 0.07 rad/s) of the FWT system in the sway mode, as shown in Figure 13(c) and 13(d). The reason for the excitation of the sway resonant response is analogous to that of the surge in Figure 12(a) and (b). As a consequence, a resonance at the sway resonant frequency (ω = 0.0644 rad/s) is also excited in the platform roll motion, which can be confirmed from Figure 13(g) and 13(h). It is because of the strong coupling between the platform sway motion and the roll

motion. With the existence of the fluid viscosity, the amplitudes of these platform motion time series are effectively decreased, as well as the resonant response peaks in their spectrums.

7. Conclusions

This paper presents a time-domain method for modeling the dynamics of an FWT with multiple rotors on the deck of a semi-submersible floating platform. It is particularly noticed that the floating foundation is a truss structure consisting of many slender braces. Such slim members can bring a significant effect of the viscous wave damping, which is caused by the wave drag force upon those members.

A systematic methodology of modeling such a floating truss structure is established based on the proposed time-domain hybrid panel-stick method, combining the potential flow theory for large-diameter structures with the Morison strip method for small-diameter structures. In the meantime, an efficient tool has been developed to deal with a set of slender cylindrical members in arbitrary lengths, diameters, orientations, and locations. The tool includes a stick mesh generator and a Morison dynamic solver. The Morison dynamic solver has been incorporated into the time-domain solver for the FWT dynamics. The developed methodology and software are then applied to an FWT developed in Kyushu University. It is validated with an experiment in regular waves in the wave tank of RIAM, Kyushu University. The simulation results are in good agreement with the experimental data, confirming the validity of the developed method for the FWT. Further numerical simulations are carried out under a set of wind and wave conditions. Comparisons are made between the parked wind turbine and the operating wind turbine and between simulations with and without the viscous damping.

It is found that in all cases of conditions without consideration of the wave drag force, the platform has a resonant response occurring at the resonant frequency of each DoF. The resonant frequencies are close to the natural frequencies of the FWT system with moorings. In addition to the resonant response, the wave-induced response is always excited, whose peak frequency coincides with that of the incident wave spectrum. However, in the presence of viscous damping, the peak value of wave-induced response can be slightly reduced. With the effect of viscous damping, which is evaluated by the Morison dynamic solver, the resonant response of each DoF can be suppressed. It means that the energy of resonant response dissipates with the fluid viscosity. In the presence of steady wind, the translational surge or sway motion can be significantly excited at its resonance frequency, in comparison to the case when the wind turbine is parked. It is mainly due to the work that the wind has done to the FWT, which enhances remarkably the total kinetic energy of the platform and, therefore, increases the translational velocity of the platform in the surge or sway DoF at the equilibrium position. An additional resonant response due to the sway or surge resonance is excited as well in the rotational platform motion of the roll or pitch DoF. It can be attributed to the strong couplings between the sway and the roll motions and between the surge and the pitch motions. These findings are believed to be of great importance to the design and operation of such FWT systems.

Acknowledgment: The authors thank the anonymous referees for their constructive comments during the revision process.

Funding: The first author is also grateful to the financial support from the Open Research Fund (Grant Number LP1815) of the State Key Laboratory of Coastal and Offshore Engineering (SKLCOE) of Dalian University of Technology, the Overseas Collaborative Research Program (Grant Number PJT-8) of the Japan Society of Naval Architects and Ocean Engineers (JASNAOE) and the Grant-in-Aid for Early-Career Scientists (JSPS KAKENHI Grant Number JP18K13939).

Conflicts of Interest: No potential conflict of interest was reported by the authors.

Nomenclature

BEM	Boundary Element Method
BEMT	Blade Element Momentum Theory

CFD	Computational Fluid Dynamics
DOF	Degree of Freedom
FWT	Floating Wind Turbine
HAMS	Hydrodynamic Analysis of Marine Structures
JONSWAP	Joint North Sea Wave Observation Project
MAP++	Mooring Analysis Program
MSL	Mean Sea Level
N-S	Navier-Stokes
P-M	Pierson-Moskowitz
RAO	Response Amplitude Operator
RIAM	Research Institute for Applied Mechanics
TLP	Tension Leg Platform
WAFO	Wave Analysis for Fatigue and Oceanography
WINFLO	Wind turbine with INnovative design for Floating Lightweight Offshore

573

574 **References**

575 1. Bae, Y. H., Kim, M. H., 2014. Coupled dynamic analysis of multiple wind turbines on a large single
576 floater. *Ocean Engineering*, 92, 175-187.
577 2. Barthelmie R., Hansen K., Frandsen S., Rathmann O., Schepers J., Schlez W., Phillips J., Rados K., Zervos
578 A., Politis E., Chaviaropoulos P., 2009. Modelling and measuring flow and wind turbine wakes in large
579 wind farms offshore. *Wind Energy* 12(5):431-44.
580 3. Barthelmie R., Larsen G., Frandsen S., Folkerts L., Rados K., Pryor S., Lange B., Schepers G., 2006. *Journal*
581 Comparison of wake model simulations with offshore wind turbine wake profiles measured by sodar. *of*
582 *Atmospheric and Oceanic Technology* 23(7):888-901.
583 4. Bayati, I., Jonkman, J., Robertson, A., Platt, A., 2014. The effects of second-order hydrodynamics on a semi-
584 submersible floating offshore wind turbine. In: *Journal of Physics: Conference Series* (Vol. 524, No. 1, p.
585 012094). IOP Publishing.
586 5. Benitz M., Lackner M., Schmidt D., 2015. Hydrodynamics of offshore structures with specific focus on wind
587 energy applications. *Renewable and Sustainable Energy Reviews* 44:692-716.
588 6. Boulluec M. Le, Ohana J., Martin A., Houmard A., 2013. Tank testing of a new concept of floating offshore
589 wind turbine, in: *Proc. 32nd International Conference on Ocean, Offshore and Arctic Engineering*, Nantes, France.
590 7. Brodtkorb, P., Johannesson, P., Lindgren, G., Rychlik, I., Rydén, J., Sjö, E., 2000. WAFO - a Matlab toolbox
591 for analysis of random waves and loads. *Proceedings of the 10th International Offshore and Polar Engineering*
592 *Conference*, Seattle.
593 8. Chen X., 2004. Hydrodynamics in offshore and naval applications - Part I. In: *Proc. Of the 6th Intl. Conf.*
594 *Hydrodynamics*, Perth, Australia.
595 9. Faltinsen O., 1993. *Sea loads on ships and offshore structures*. Cambridge: Cambridge University Press.
596 10. Goupee A., Koo B., Kimball R., Lambrakos K., Dagher H., 2014. Experimental comparison of three floating
597 wind turbine concepts. *Journal of Offshore Mechanics and Arctic Engineering* 136(2): 020906.
598 11. Hansen M., 2015. *Aerodynamics of wind turbines*. Routledge.
599 12. Hu C., Sueyoshi M., Liu C., Liu Y., 2014. Hydrodynamic analysis of a semi-submersible type floating wind
600 turbine. *Journal of Ocean and Wind Energy* 1(4): 202-208.
601 13. Ishihara, T., Zhang, S., 2019. Prediction of dynamic response of semi-submersible floating offshore wind
602 turbine using augmented Morison's equation with frequency dependent hydrodynamic coefficients.
603 *Renewable Energy*, 131, 1186-1207.
604 14. Jensen, N., 1983. *A note on wind generator interaction*. Technical Report from the Risø National Laboratory
605 (Risø-M-2411), Roskilde, Denmark.
606 15. Jonkman, J., 2007. *Dynamics Modeling and Loads Analysis of an Offshore Floating Wind Turbine*; University of
607 Colorado at Boulder: Boulder, CO, USA; Volume 3, ISBN 0070378460.
608 16. Jonkman J., 2009. Dynamics of offshore floating wind turbines—model development and verification. *Wind*
609 *Energy* 12(5):459-92.
610 17. Karimirad, M., Michailides, C., 2015. V-shaped semi-submersible offshore wind turbine: An alternative
611 concept for offshore wind technology. *Renewable Energy*, 83, 126-143.

18. Karimirad, M., Michailides, C., 2016. V-shaped semi-submersible offshore wind turbine subjected to misaligned wave and wind. *Journal of Renewable and Sustainable Energy*, 8(2), 023305.
19. Katic, I., Højstrup, J., Jensen, N., 1986. *A simple model for cluster efficiency*. In European Wind Energy Association Conference and Exhibition.
20. Kim, H. C., Kim, K. H., Kim, M. H., Hong, K., 2017. Global performance of a KRISO semi-submersible multiunit floating offshore wind turbine: Numerical simulation vs. model test. *International Journal of Offshore and Polar Engineering*, 27(01), 70-81.
21. Koch, C., Lemmer, F., Borisade, F., Matha, D., Cheng, P. W., 2018. Validation of INNWIND. EU scaled model tests of a semi-submersible floating wind turbine. *International Journal of Offshore and Polar Engineering*, 28(01), 54-64.
22. Kvittem, M. I., Bachynski, E. E., Moan, T., 2012. Effects of hydrodynamic modelling in fully coupled simulations of a semi-submersible wind turbine. *Energy Procedia*, *24*, 351-362.
23. Leblanc L., Petitjean F., Roy F., Chen X., 1993. A mixed panel-stick hydrodynamic model applied to fatigue life assessment of semi-submersibles. *Proceedings of 12th International Conference on Ocean, Offshore and Arctic Engineering*, Glasgow, Scotland.
24. Ledru, R., Le Cunff, C., Heurtier, J. M., Perdrizet, T., Poirette, Y., 2014. Influence of Hydrodynamic Modeling Assumptions on Floating Wind Turbine Behaviour. *Proceedings of 33rd International Conference on Ocean, Offshore and Arctic Engineering*.
25. Li B, Liu K, Yan G, Ou J., 2011. Hydrodynamic comparison of a semi-submersible, TLP, and Spar: numerical study in the South China Sea environment. *J. Mar. Sci. Appl.* 10: 306–14.
26. Li, L., Gao, Y., Hu, Z., Yuan, Z., Day, S., Li, H., 2018. Model test research of a semi-submersible floating wind turbine with an improved deficient thrust force correction approach. *Renewable energy*, 119, 95-105.
27. Li, Y., Teng, B., 2002. *Wave action on maritime structures (in Chinese)*. Ocean Press, Beijing.
28. Li, Y., Yu, Y. H., 2012. A synthesis of numerical methods for modeling wave energy converter-point absorbers. *Renewable and Sustainable Energy Reviews*, 16(6), 4352-4364.
29. Liu, Y., Hu, C., Sueyoshi, M., Yoshida, S., Honda, Y., Ohya, Y., 2014. Time domain simulation of a semi-submersible type floating wind turbine. *Proceedings of 24th International Ocean and Polar Engineering Conference*, Busan, Korea.
30. Liu, Y., Li, S., Yi, Q., Chen, D., 2016a. Developments in semi-submersible floating foundations supporting wind turbines: A comprehensive review. *Renew. Sustain. Energy Rev.* 60: 433–449.
31. Liu Y., Hu C., Sueyoshi M., Iwashita H., Kashiwagi M., 2016b. Motion response prediction by hybrid panel-stick models for a semi-submersible with bracings. *Journal of Marine Science and Technology* 21(4):742-57.
32. Liu Y., Yoshida S., Hu C., Sueyoshi M., Sun L., Gao J., Cong P., He G., 2018a. A reliable open-source package for performance evaluation of floating renewable energy systems in coastal and offshore regions. *Energy Conversion and Management* 174: 516-536.
33. Liu, Y., Yoshida, S., Yamamoto, H., Toyofuku, A., He, G., Yang, S. 2018b. Response Characteristics of the DeepCwind Floating Wind Turbine Moored by a Single-Point Mooring System. *Applied Sciences*, *8*(11), 2306.
34. Liu, Y., Li, S., Chan, P. W., Chen, D., 2018c. On the Failure Probability of Offshore Wind Turbines in the China Coastal Waters Due to Typhoons: A Case Study Using the OC4-DeepCwind Semisubmersible. *IEEE Transactions on Sustainable Energy*, 10(2), 522-532.
35. Liu Y., 2019. HAMS: A Frequency-Domain Preprocessor for Wave-Structure Interactions—Theory, Development, and Application. *Journal of Marine Science and Engineering*, 7(3), 81.
36. Masciola, M., 2013a. *Instructional and Theory Guide to the Mooring Analysis Program*. NREL. Available online: https://nwtc. nrel. gov/system/files/MAP_v0, 87 (accessed on 25 Feb 2019).
37. Masciola, M.; Jonkman, J.; Robertson, A., 2013b. Implementation of a multi-segmented, quasi-static cable model. In *Proceedings of the Twenty-third International Offshore and Polar Engineering Conference*, Anchorage, AK, USA.
38. Masciola M., 2015. MAP++ Python Wrapper. https://map-plus-plus.readthedocs.io/en/latest/python_example.html (accessed on 13 May 2020).
39. Moriarty P., Hansen A., 2005. *AeroDyn theory manual*. National Renewable Energy Lab., Golden, CO (US).
40. Nematbakhsh, A., Bachynski, E. E., Gao, Z., Moan, T., 2015. Comparison of wave load effects on a TLP wind turbine by using computational fluid dynamics and potential flow theory approaches. *Applied Ocean Research*, 53, 142-154.

41. Newman J.N., 1999. *Heave response of a semi-submersible near resonance*. Proceedings of 14th International Workshop on Water Waves and Floating Bodies, Port Huron, USA.
42. Ran, Z., 2000. *Coupled dynamic analysis of floating structures in waves and currents*. Doctoral dissertation, Texas A&M University.
43. Robertson, A., Jonkman, J.M., Masciola, M., Song, H., Goupee, A., Coulling, A., Luan, C., 2014. *Definition of the Semisubmersible Floating System for Phase II of OC4*; National Renewable Energy Laboratory (NREL): Golden, CO, USA.
44. Robertson, A. N., Wendt, F., Jonkman, J. M., Popko, W., Dagher, H., Gueydon, S., ... & Soares, C. G., 2017. OC5 project phase II: validation of global loads of the DeepCwind floating semi-submersible wind turbine. *Energy Procedia*, 137, 38-57.
45. Roddier, D., Cermelli, C., Aubault, A., Weinstein, A., 2010. WindFloat: A floating foundation for offshore wind turbines. *J. Renew. Sustain. Energy 2*: 033104.Sarpkaya T., 2010. *Wave forces on offshore structures*. Cambridge: Cambridge University Press.
46. Spera, D., 1994. *Wind Turbine Technology*, ASME Press, New York.
47. Tran, T. T., Kim, D. H., 2015. The coupled dynamic response computation for a semi-submersible platform of floating offshore wind turbine. *Journal of wind engineering and industrial aerodynamics*, 147, 104-119.
48. Uzunoglu, E., Soares, C. G., 2018. On the model uncertainty of wave induced platform motions and mooring loads of a semi-submersible based wind turbine. *Ocean Engineering*, 148, 277-285.
49. Wang, K., Ji, C., Xue, H., & Tang, W., 2016. Fatigue damage characteristics of a semisubmersible-type floating offshore wind turbine at tower base. *Journal of Renewable and Sustainable Energy*, 8(5), 053307.
50. Wendt, F. F., Robertson, A., Jonkman, J. M., Hayman, G., 2015. *Verification of new floating capabilities in FAST v8*. In 33rd Wind Energy Symposium (p. 1204).
51. Wikipedia, 2020a. https://en.wikipedia.org/wiki/Newmark-beta_method (accessed on 8 May 2020).
52. Wikiversity,2020b. https://en.wikiversity.org/wiki/Adams-Bashforth_and_Adams-Moulton_methods (accessed on 8 May 2020).
53. Wikipedia, 2020c. https://en.wikipedia.org/wiki/Runge%E2%80%93Kutta_methods (accessed on 8 May 2020).
54. Xiang, S., 2007. On the Filon and Levin methods for highly oscillatory integral∫ abf (x) eiωg (x) dx. *Journal of computational and applied mathematics*, 208(2), 434-439.
55. Zhu, H., Hu, C., Liu, Y., 2016. Optimum design of a passive suspension system of a semi-submersible for pitching reduction. J*ournal of Dynamic Systems, Measurement, and Control*, 138(12), 121003.